International Journal of Hydrogen Energy 61 (2024) 57–72

Contents lists available at ScienceDirect

International Journal of Hydrogen Energy

journal homepage: www.elsevier.com/locate/he

Grand Canonical Monte Carlo simulations of the hydrogen and methane storage capacities of JLU-MOF120 and JLU-MOF121

A. Granja-DelRío, I. Cabria *

Departamento de Física Teórica, Atómica y Óptica, Universidad de Valladolid, ES-47011, Valladolid, Spain

ARTICLE INFO

Keywords:
Hydrogen storage
Methane storage
Metal-organic frameworks
Grand Canonical Monte Carlo simulations

ABSTRACT

New materials that can efficiently store hydrogen and methane at high gravimetric and volumetric densities are crucial for the widespread adoption of hydrogen vehicles as an eco-friendly alternative to fossil-fueled vehicles. Metal-Organic Frameworks (MOFs) have emerged as promising candidates to meet the Department of Energy (DOE) targets for both hydrogen and methane storage. Performing Grand Canonical Monte Carlo (GCMC) simulations, the usable hydrogen and methane gravimetric and volumetric storage capacities of two recently synthesized Jilin University (JLU) MOFs have been investigated. These capacities have been compared to those of other specifically selected MOFs with similar metal compositions, with other MOF from the JLU family, as well as classical and well-established MOFs like IRMOF-15 and IRMOF-20 (IRMOF: Isoreticular Metal-Organic Framework). The two newly synthesized JLU MOFs have exhibited high usable gravimetric and volumetric storage capacities for both hydrogen and methane, at room temperature and moderate pressures ranging from 25 to 35 MPa. These capacities are comparable to or even higher than those of classical MOFs and selected MOFs with similar metal compositions.

1. Introduction

Energy is a crucial requirement for humans to perform many activities, such as warming their homes or facilitating the mobility through different modes of transportation. Furthermore, energy is not only a necessity for technological progress but also a cornerstone for ensuring humans everyday comfort. Nowadays, the primary energy consumption by source are petroleum, natural gas, coal (fossil fuels) and nuclear [1]. One of the main drawbacks is that non-renewable sources are substances that humans cannot produce and which nature takes millions of years to make them, such us petroleum or coal. Thus, non-renewable sources face the issue that their use is finite, which means they are constantly threatened by the risk of depletion due to continuous overexploitation. This fact often leads to a tendency toward an increase in the price of oil, resulting in higher costs. In addition, fossil fuels are not evenly distributed worldwide resulting in issues and disputes among countries.

Another significant issue is the environmental impact arising from their use since they are responsible for the increasing CO_2 in the atmosphere. CO_2 emissions arise primarily from the burning of fossil fuels, with transportation playing a significant role in this process. This directly contributes to the greenhouse effect and to the anthropogenic climate change. Hydrogen seems a promising solution to replace fuels in vehicles contributing to mitigate and reduce CO_2 emissions [2–5]. Hydrogen could have the potential to play a key role in achieving the goal of net-zero CO_2 emissions by 2050 [6,7]. The transition toward sustainable energy relies on various key elements including production, transportation, storage and utilization of hydrogen. When comparing it to gasoline (44 MJ/kg), hydrogen (120 MJ/kg) [8] boasts a significantly higher energy density per unit of mass. However, hydrogen shows low volumetric energy density and the storage of large quantities of hydrogen for vehicle applications remains quite challenging. The main obstacle is finding a way to store hydrogen on board allowing for a driving range exceeding 500 kilometers on a single fill, similar to current fossil fuel-based vehicles. All while considering factors such as safety, weight, volume, efficiency and cost [9–13]. The present on-board hydrogen storage includes compressing under a pressure of 700 bar [14] which lies in high cost and lower safety.

The U.S. Department of Energy (DOE) has established targets for on-board hydrogen storage systems, aiming for a requirement of 5.5 wt. % for the gravimetric capacity and 0.040 kg H_2/L for the volumetric capacity by 2025 [8,15]. These values represent the usable (deliverable or working) storage capacities. They indicate how much hydrogen can be used effectively for powering vehicles and achieving the autonomy mentioned previously. Additionally, these targets align with the idea of reversible storage, meaning that the stored hydrogen can be released and refilled repeatedly.

* Corresponding author.
E-mail address: ivan.cabria@uva.es (I. Cabria).

https://doi.org/10.1016/j.ijhydene.2024.02.311
Received 22 November 2023; Received in revised form 24 January 2024; Accepted 23 February 2024
Available online 28 February 2024

As hydrogen-powered vehicle technology advances, there appears to be a need for a transitional phase between traditional gasoline-powered cars and the widespread adoption of hydrogen-based vehicles [16]. Natural gas emerges as this viable temporary phase due to its extensive distribution network ample reserves, cost-effectiveness and relatively cleaner properties when compared to oil. The driving factor behind this choice is that the primary component of natural gas is methane, which boasts the highest hydrogen-to-carbon ratio among all fossil fuels. In contrast to coal, natural gas has the potential to significantly cut down CO_2 emissions by approximately 55%, aligning with emission reduction targets proposed by European Union [17]. This makes natural gas an appealing option for curbing environmental impacts [18,19]. Methane presents high gravimetric capacity in contrast with its low volumetric capacity at ambient conditions. As in the hydrogen case, storage continues to be a substantial obstacle. Typically, natural gas for on-board vehicle use is either compressed or liquefied. Both methods are also used in hydrogen storage. Yet, both compression and liquefaction techniques demand expensive and space-intensive storage systems [20,21]. The Advanced Research Projects Agency - Energy (ARPA-E) of the DOE, has set storage targets to provide guidance for research on methane storage: a volumetric capacity of 0.250 kg of methane per liter and a gravimetric capacity of 0.5 g/g or 33.33 wt. % at room temperature and low or moderate pressures [20–24].

Besides the methods of compression and liquefaction, an alternative way to store methane or hydrogen is in solid-state storage systems. This method is a booming technology which combines low and moderate pressures (≤ 25–35 MPa) and may be achieved at room temperature unlike the other two methods [24,25]. This decrease in pressure enables the use of lightweight, cost-effective and conformable fuel containers. Solid-state storage entails the utilization of either metal hydrides [26–30] or solid porous materials [31–35]. In the former, gas is absorbed within the voids or interstitial spaces of the materials. Diverse compounds such as AB, AB_2, A_2B, and others find application in gas storage. Notably, MgH_2 stands out as a particularly advantageous metal-hydride storage material [36–39]. On the other hand, adsorbed gas storage involves the use of solid porous materials for physisorption where the tank is filled with solid porous materials and the gas is stored inside their pores. The success of adsorbed gas technology relies on the development of effective adsorbent materials. Different groups of porous materials have been extensively investigated and assessed as potential storage media for methane and hydrogen [40–57].

In recent years, metal–organic frameworks (MOFs) have gained significant attention as a novel category of porous materials. MOFs consist of metal ions or clusters, often referred to as secondary building blocks or SBUs, connected by organic ligands, forming intricate 3D networks [58]. The extensive variety of potential organic linkers, combined with a wide array of metal ions and clusters, gives rise to a vast range of porous materials [59]. These materials exhibit diverse pore surface properties and chemically adjustable structures, making them suitable for a wide array of applications, specifically gas storage, for example, hydrogen and natural gas [60–70].

The adsorption properties of MOFs [71], such as their ability to store hydrogen and methane, have been thoroughly investigated through several experimental researches [63,72–78] and simulations [75,79–89] during the last decades, including the commonly employed Grand Canonical Monte Carlo (GCMC) method [41–44,75,90–92].

Lately, a group of the Jilin University (JLU) [93], published the synthesis of two JLU MOFs with high-valency metal ions, Bi for JLU-MOF120 and In for JLU-MOF121, and with carboxylate-based ligands forming twofold interpenetrated structures. Zhu et al. [93] changed the torsion angles of the ligand, and thus, the degrees of interpenetration for JLU-MOF120 and JLU-MOF121 are disparate and lead to different properties.

The aim of this investigation is to calculate the usable hydrogen and methane storage capacities of these JLU MOFs at room temperature, which show considerable potential as storage materials. The GCMC simulations have been carried out to calculate the usable storage capacities of the two synthesized JLU MOFs under room temperature conditions and within a pressure range spanning from 0.5 to 35 MPa.

Table 1
Parameters of the SRK equation of state of hydrogen and methane: ω, P_c in MPa and T_c in K.

Gas	ω	P_c	T_c	Source
H_2	−0.216	1.28	33.2	Zhou and Zhou [96]
CH_4	0.01142	4.5992	190.56	Xu et al. [97]

These newly synthesized MOFs are Bi and In-based and hence, to gain deeper insights, GCMC simulations of the usable storage capacities of Bi, In, Al, P and Sb-based MOFs with the same or similar C/metal ratio as the two JLUs have been also undertaken. The usable storage capacities of the JLUs and the selected metal-based (Bi, In, Al, P and Sb) MOFs have been analyzed and compared with the usable storage capacities of widely recognized classical MOFs. Additionally, the relationship between the usable storage capacities and the structural properties (porosity, density and pore size) of all the simulated MOFs have been investigated. This understanding and foresight of the interactions between the adsorbed molecules and MOFs are essential to understand the origin of the storage capacities and for the design of novel metal–organic frameworks. Throughout this paper, unless otherwise stated, the term storage capacities refers to usable storage capacities.

2. Methodology

2.1. Simulations parameters and details

Grand Canonical Monte Carlo (GCMC) simulations have been carried out at room temperature (298.15 K) and pressures in a range of 0.5 to 35 MPa. The GCMC method employs the grand canonical ensemble to change the number of molecules involved in the simulation. For each GCMC simulation, a total of ten million iterations were performed. To ensure equilibrium was reached, five million iterations were dedicated to the equilibrium process. The remaining iterations were utilized to determine the gravimetric and volumetric storage capacities for both hydrogen and methane.

The simulations were carried out utilizing an in-house code, named in this work as mcmgs. The Metropolis algorithm [94] was employed in each iteration. Within each iteration, three types of potential changes or moves were considered. Approximately 20% of the trials involved the movement of a molecule, allowing for spatial repositioning within the system. Another 40% of the trials focused on molecule deletion. The remaining 40% of the trials encompassed molecule insertion, mimicking the addition of a molecule into the MOF. The selection of these percentages was determined through extensive testing and optimization, aiming to achieve effective sampling and accurate representation of the system's behavior. In the GCMC simulations, the chemical potential was derived from the widely utilized Soave–Redlich–Kwong (SRK) equation of state [95]. The dimensionless acentric factor (ω), critical pressure (P_c) and critical temperature (T_c) values for hydrogen and methane were obtained from Zhou and Zhou [96] and Xu et al. [97], respectively. These values can be found in Table 1.

To simulate the interactions between gas molecules (H_2 or CH_4) and the atoms of the MOFs, the Lennard-Jones (LJ) interaction potential energies [98] were employed. The LJ potential provides a mathematical framework for describing the intermolecular forces and interactions involved in the system. It follows the well-known Lennard-Jones equation, which captures both the attractive and repulsive components of the interactions between the gas molecules and the atoms of the MOFs. The Lennard-Jones interaction potential energy has the following formula:

$$V = 4\epsilon\left[\left(\frac{\sigma}{r}\right)^{12} - \left(\frac{\sigma}{r}\right)^{6}\right], \quad (1)$$

where ϵ, σ and r in Eq. (1) are the LJ well depth ($\epsilon > 0$), the distance at which the potential energy function between the two particles is

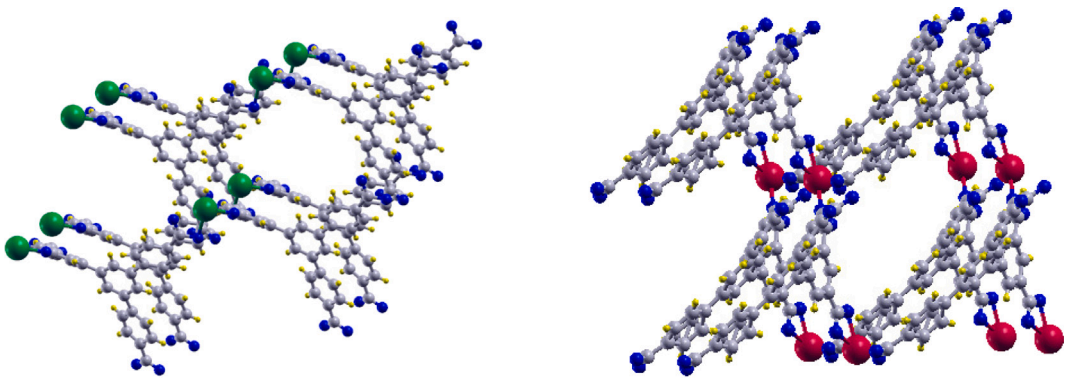

Fig. 1. Simulation cells of JLU-MOF120 and JLU-MOF121 (left and right panels, respectively). Oxygen, carbon, hydrogen, bismuth and indium atoms are represented by blue, gray, yellow, green and red balls, respectively. (For interpretation of the references to color in this figure legend, the reader is referred to the web version of this article.)

Table 2
Lennard-Jones coefficients σ (in Å) and ϵ (in eV) of the molecules and the atoms of the MOFs studied in the present GCMC simulations.

Atom or molecule	σ	ϵ	Source
Ag	2.644	0.345000	Guan et al. [104]
Al	2.574	0.507220	Filippova et al. [105]
Au	2.934	0.001691	Rappé et al. [106]
Bi	3.050	0.059000	Arkundato et al. [107]
Cl	3.350	0.014951	Singer et al. [108]
Co	2.499	0.051859	Sebesta et al. [109]
Cu	2.297	0.520310	Filippova et al. [105]
F	3.217	0.005419	Reif et al. [110]
Ga	3.905	0.017994	Rappé et al. [106]
H_2	2.970	0.002870	Rzepka et al. [101]
H	2.846	0.000659	Mayo et al. [111]
In	2.810	0.052290	Tribe et al. [112]
K	3.262	0.003965	Reif et al. [110]
Li	2.051	0.013225	Ponce et al. [113]
Mo	2.489	0.151000	Mardiyah et al. [114]
N	3.310	0.003214	Cheung et al. [115]
O	3.033	0.004150	Mayo et al. [111]
CH_4	3.730	0.012748	Jorgensen et al. [116]
P	3.656	0.019100	Mardiyah et al. [114]
Sb	3.938	0.019469	Rappé et al. [106]
S	3.590	0.014916	Mayo et al. [111]
Y	2.980	0.003122	Rappé et al. [106]
Zn	0.998	0.008291	Soper et al. [117]
Zr	2.910	0.735981	Beyer et al. [118]
C-H_2	3.190	0.002628	Rzepka et al. [101]

zero and the distance between the two particles, respectively. The values of the ϵ and σ coefficients depend on each particle involved in the interaction. The ϵ and σ coefficients of the interactions between different particles have been obtained using the Berthelot [99] and the Good–Hope [100] combining rules, respectively.

Table 2 shows the values for ϵ and σ coefficients of the atoms and molecules used in the present GCMC simulations. The LJ coefficients of the C–H_2 interaction used in these simulations were obtained from Rzepka et al. [101]. The LJ parameters of the rest of the interactions have been obtained by means of the above-mentioned Good–Hope–Berthelot combining rule. To include quantum effects in the interaction potential, the Feynman–Hibbs correction has been used [102]. All the present GCMC simulations have been performed using this quantum correction. The cutoff radius for the LJ interaction potential was 20 and 7.5 Å for H_2 and CH_4 interactions, respectively. These values were obtained from several trials, as indicated in prior studies [42,43]. Docherty et al. [103] reported a similar cutoff of 9 Å for methane.

2.2. Sets of MOFs and simulation cells

Four sets of MOFs have been simulated: (a) The JLU-MOF120, a Bi-based MOF, and the JLU-MOF121, an In-based MOF [93], (b) a set of 21 classical MOFs, (c) a set of selected Bi and In-based MOFs with C/metal ratios similar to those of the two JLUs and (d) a set of 23 JLU MOFs (rest-JLU). The third set includes also MOFs based on metal atoms in the same column of the periodic table as Bi (P and Sb) and In (Al) (see Table 3). The fourth group comprises MOFs synthesized at Jilin University.

Table 3
Ratios C/metal of the JLU MOFs, the selected Bi, In, Al, P, Sb-based MOFs and the two best classical MOFs. IRMOF stands for Isoreticular Metal-Organic Frameworks.

MOF	Ratio C/metal	MOF	Ratio C/metal
JLU-MOF120	C/Bi = 28.0	CUSQEP	C/Bi = 29.0
IZUKIZ	C/Bi = 27.0	HOJJAU	C/P = 29.0
QOXQIG	C/P = 29.0	DIFZAW	C/P = 28.5
QECHOY	C/P = 28.0	QOXQEC	C/P = 28.0
QAPZUF	C/P = 26.0	FAGMAE	C/Sb = 30.0
JLU-MOF121	C/In = 30.0	CAJWAN	C/In = 30.0
FAHQIQ	C/In = 30.0	GALHUY	C/In = 28.0
IFIPEV	C/In = 28.0	ROLRES	C/In = 28.0
XEJTIR	C/Al = 28.0		
IRMOF-15	C/Zn = 12.0	IRMOF-20	C/Zn = 7.5
JLU-Liu39	C/Cu = 7.6	JLU-Liu30	C/Cu = 16.4

The MOFs of the third set were selected from the Cambridge Crystallographic Database Center (CCDC) [119], more specifically, from the MOF CCDC subset [120]. That subset contains a few Bi-based and In-based MOFs. The C/Bi and C/In ratios of those two JLU MOFs and of the Bi and In-based MOFs of the subset were calculated. JLU-MOF120 has C/Bi ratio of 28 and JLU-MOF121 possesses a C/In ratio of 30 (see Table 3). Only two Bi-based and five In-based MOFs were found with similar ratios as the two JLU MOFs. To broaden the pool of MOFs for comparison with the JLUs, MOFs based on metals in the same column of the periodic table as Bi and In, and with a C/metal ratio similar to that of the JLUs were selected. One Al-based, six P-based and one Sb-based MOFs were found with those characteristics.

The GCMC simulations of all the MOFs of the four sets were performed at the same temperature, pressures and conditions as mentioned before, allowing for a meaningful evaluation and comparison of their respective usable storage capacities.

The simulation cells of the MOFs of the four sets (JLUs, classical, selected and rest-JLUs) were acquired from their respective files in the Crystallographic Information File (CIF) format, which are available in the CCDC database [119]. The simulation cells of the two JLU MOFs have been plotted in Fig. 1, using the xcrysden code [121]. The group of 21 classical MOFs includes IRMOF-1 to IRMOF-20 (excluding numbers 10, 13, 17 and 19), HKUST-1, MOF-177, NU-111, NU-125 and ZIF-8. The set rest-JLUs includes CJLU-1, JLU-Liu4, JLU-Liu8, JLU-Liu9, JLU-Liu10, JLU-Liu20, JLU-Liu29, JLU-Liu30, JLU-Liu33, JLU-Liu33F, JLU-Liu39, JLU-Liu44, JLU-Liu44.0, JLU-Liu45, JLU-Liu46, JLU-Liu47, JLU-MOF48, JLU-MOF49, JLU-MOF51, JLU-MOF59, JLU-MOF110, JLU-MOF11, JLU-MOF112 and JLU-MOF201-Y.

2.3. Calculation of the porosity and pore radius

The porosity is determined by assessing the relationship between the available volume and the total volume of the simulation cell of a MOF. It is a dimensionless magnitude. Specifically, the available volume for a gas molecule is the difference between the volume of the simulation cell, denoted as V, and the volume occupied by the constituent atoms of the MOF, V_{occ}.

To calculate the volume V_{occ}, a grid of n points in the simulation cell is created. The number of grid points located inside the sphere of an atom of the simulation cell is represented by ni. Then, the volume V_{occ} is determined by the product of the simulation cell's volume, V, and the ratio of the sum of these grid points, ni, to the total number of points, n, this is Vni/n. The radius of an atom, r, is equivalent to the interaction distance $\sigma(atom, molecule)$. The volume of an atom's sphere can be calculated as $4\pi r^3/3$. The LJ interaction potential energy becomes zero when the distance between an atom and a molecule equals $\sigma(atom, molecule)$. Due to this definition of the radius of an atom interacting with a molecule, the magnitudes available volume, volume occupied by the atoms and porosity depend on the type of gas molecule.

An algorithm was used to find the pores of the MOFs with a radius equal to or greater than 3 Å. Hydrogen and methane molecules do not fit into pores with a smaller radius. The algorithm generates, in the first step, a three-dimensional grid of points within the simulation cell. The distance between the grid points is 1.0 Å. The second step consists on calculating, for each grid point i, the distance d_{ij} from the grid point i to every atom j in the simulation cell. Then, the minimum distance, $dmin(i)$, of the d_{ij} set of distances is calculated.

The third step of the algorithm consists on calculating the pore radii using the set of $dmin(i)$ distances. The radius of the first pore is the largest $dmin(i)$. The corresponding grid point i is the center of the pore. The set of $dmin(i)$ values is then recalculated. The grid points contained within the first pore are treated as 'atoms' within the MOF structure. The second and third steps are repeated to obtain a new set of $dmin(i)$ distances and to obtain the second, the third pore, etc. The process continues until the largest $dmin(i)$ is smaller than 3 Å. The algorithm calculates a set of pore radii, along with the average pore radius. The first pore radius obtained using this algorithm is the largest pore radius of the MOF. The spherical pores obtained using this algorithm do not overlap.

2.4. Definitions of the storage capacities

The GCMC simulations have been utilized to simulate the total gravimetric and volumetric storage capacities for both hydrogen and methane [4,10,67]. The total volumetric storage capacity, v_c, often referred to as the density of stored hydrogen or methane, is formally defined as follows:

$$v_c = \frac{M_g}{V} , \tag{2}$$

where V is the volume of the simulation cell and M_g is the mass of stored gas, whether it is hydrogen or methane, in the simulation cell. In this paper, v_c is calculated in kg of gas (either hydrogen or methane) per liter. Total (hydrogen or methane) gravimetric storage capacity, g_c, is defined by

$$g_c = \frac{100 M_g}{M_g + M_{ads}} , \tag{3}$$

where M_{ads} stands for the mass of the solid porous adsorbent material within the simulation cell. Consequently, the units for the total gravimetric capacity are computed in weight percentage (wt. %) units.

The amount of gas (either hydrogen or methane) that can be effectively used at a given pressure P and temperature T, $M_{ug}(P,T)$, known as usable mass of gas (See Eq. (4)), is determined by the difference between the total mass of gas stored at P and T and the total mass of gas stored at the depletion pressure, P_{dep}, (also known as minimum or back pressure) and at the same temperature T [4,8,15,67]. The quantity of hydrogen that continues being adsorbed within the material under the back pressure significantly constrains the effective capacity of these materials.

$$M_{ug}(P,T) = M_g(P,T) - M_g(P_{dep},T) . \tag{4}$$

The usable (hydrogen or methane) volumetric and gravimetric capacities are calculated by Eqs. (2) and (3), respectively, introducing the usable mass of gas stored $M_{ug}(P,T)$ in place of $M_g(P,T)$:

$$v_c(P,T) = \frac{M_{ug}(P,T)}{V} , \tag{5}$$

$$g_c(P,T) = \frac{100 M_{ug}(P,T)}{M_{ug}(P,T) + M_{ads}} . \tag{6}$$

The units of the usable capacities are the same as those of the total capacities. The depletion pressure, P_{dep}, used in this work is 0.5 MPa. Only the usable storage capacities, Eqs. (5) and (6), will be employed in this paper, except when specified otherwise.

2.5. Comparison of hydrogen and methane storage capacities with experimental results

The excess adsorption is the amount of gas contained in the sample pores less the amount of gas that would be present in the pores in the absence of gas–solid intermolecular forces. Excess adsorption capacity is a material property; thus it is what is usually reported in the scientific literature and can be used to compare different materials.

Tables 4 and 5 presents an overview of the total and excess storage capacities for both hydrogen and methane within a selection of classical MOFs, with a particular emphasis on IRMOF-1 (See Table 4). This comparison involves an assessment of simulations conducted with the mcmgs code against experimental data from other research groups, all conducted under comparable ambient temperatures.

In the realm of hydrogen storage, the gravimetric and volumetric capacities calculated using the mcmgs code demonstrate only minimal deviations from experimental results. Generally, the mcmgs-derived capacities are only slightly higher, ranging around 19%–28% compared to the experimentally obtained values.

In the case of methane, the comparative analysis between experimental data and mcmgs simulations reveals remarkable similarity. For pressures below 8 MPa, experimental total gravimetric capacities show a slight elevation of approximately 10% compared to those derived from mcmgs simulations. Beyond 8 MPa, mcmgs simulations tend to yield values about 20% higher than experimental results. Discrepancies in total volumetric capacities between experimental and mcmgs-simulated values are relatively modest, around 10%.

To facilitate a thorough comparison between experimental findings and mcmgs simulations, data from two distinct experimental studies, namely Yang et al. [124] and Langmi et al. [125], were incorporated. The mcmgs calculations were meticulously conducted under identical conditions, precisely at the same temperature (298 K) and corresponding pressures as detailed in both referenced studies. The hydrogen excess gravimetric capacities have been graphically represented against pressure in Fig. 2. For lower pressure values, a remarkable convergence is observed between experimental data from Yang et al. and mcmgs simulations, with a near-equivalence. However, as pressure levels increase, a discernible deviation emerges, accounting for only a 16% divergence. Disparities between values from Langmi et al. and mcmgs simulations are slightly more pronounced across all pressure levels.

Table 4
Total storage capacities of hydrogen and methane in IRMOF-1 under diverse temperature and pressure conditions. The results incorporate both experimental data from external research groups and simulated mcmgs values derived from simulations conducted in this work. Pressure (P) is expressed in megapascals (MPa), temperature (T) in Kelvin (K), gravimetric capacity (g_c) in weight percentage (wt. %), and volumetric capacity (v_c) in kilograms per liter (kg/L). The term "Type" denotes the nature of the storage capacity being considered.

MOF	Gas	P	T	Technique	g_c	v_c	Type	Source
IRMOF-1	H_2	6	300	exps.	0.30		Excess	[122]
IRMOF-1	H_2	6	300	mcmgs	0.37		Excess	
IRMOF-1	H_2	6	298	exps.	0.45		Excess	[123]
IRMOF-1	H_2	6	298	mcmgs	0.38		Excess	
IRMOF-1	H_2	10	298	exps.	0.45		Excess	[124]
IRMOF-1	H_2	10	298	mcmgs	0.58		Excess	
IRMOF-1	H_2	10	298	exps.	0.42		Excess	[125]
IRMOF-1	H_2	10	298	mcmgs	0.58		Excess	
IRMOF-1	CH_4	3.6	300	exps.	13.5	0.0787	Total	[122]
IRMOF-1	CH_4	3.6	300	mcmgs	12.3	0.0837	Total	
IRMOF-1	CH_4	10	298	exps.	14.7		Excess	[126,127]
IRMOF-1	CH_4	10	298	mcmgs	18.5		Excess	
IRMOF-1	CH_4	3.5	298	exps.	14.2		Total	[126,128]
IRMOF-1	CH_4	3.5	298	mcmgs	12.1		Total	
IRMOF-1	CH_4	3.5	298	exps.	11.7		Excess	[126,129]
IRMOF-1	CH_4	3.5	298	mcmgs	11.1		Excess	

Table 5
Total storage capacities of hydrogen and methane in classical MOFs under diverse temperature and pressure conditions. The results incorporate both experimental data from external research groups and simulated mcmgs values derived from simulations conducted in this work. Pressure (P) is expressed in megapascals (MPa), temperature (T) in Kelvin (K), gravimetric capacity (g_c) in weight percentage (wt. %), and volumetric capacity (v_c) in kilograms per liter (kg/L). The term "Type" denotes the nature of the storage capacity being considered.

MOF	Gas	P	T	Technique	g_c	v_c	Type	Source
MOF-177	CH_4	10	298	exps.	18.1		Total	[126,127]
MOF-177	CH_4	10	298	mcmgs	22.2		Total	
IRMOF-14	CH_4	3.5	298	mcmgs	15.7		Total	[127,130]
IRMOF-14	CH_4	3.5	298	mcmgs	15.0		Total	
HKUST-1	CH_4	6.5	298	exps.	17.8	0.1910	Total	[54]
HKUST-1	CH_4	6.5	298	mcmgs	15.4	0.1724	Total	
HKUST-1	CH_4	6.5	298	exps.	15.1	0.1574	Excess	[54]
HKUST-1	CH_4	6.5	298	mcmgs	14.8		Excess	
NU-125	CH_4	6.5	298	exps.	22.3	0.1659	Total	[54]
NU-125	CH_4	6.5	298	mcmgs	20.5	0.1570	Total	
NU-125	CH_4	6.5	298	exps.	18.2	0.1295	Excess	[54]
NU-125	CH_4	6.5	298	mcmgs	19.0		Excess	
Al-nia-MOF-1	CH_4	8	258	exps.	28.6	0.1880	Total	[131]
Al-nia-MOF-1	CH_4	8	258	mcmgs	29.1	0.2010	Total	[41]
Al-nia-MOF-1	CH_4	8	273	exps.	24.5	0.1660	Total	[131]
Al-nia-MOF-1	CH_4	8	273	mcmgs	27.6	0.1870	Total	[41]
Al-nia-MOF-1	CH_4	8	298	exps.	23.1	0.1420	Total	[131]
Al-nia-MOF-1	CH_4	8	298	mcmgs	24.8	0.1610	Total	[41]
Al-nia-MOF-1	CH_4	8	298	exps.	21.3	0.1230	Usable	[131]
Al-nia-MOF-1	CH_4	8	298	mcmgs	22.1	0.1390	Usable	[41]

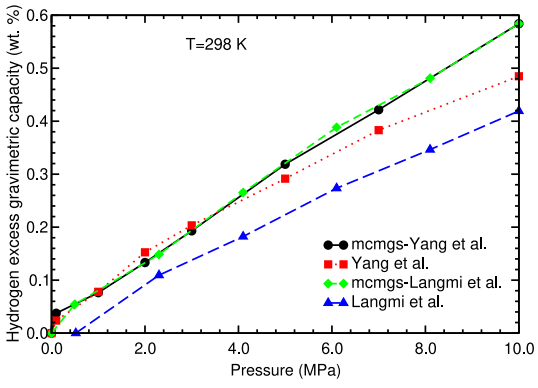

Fig. 2. Excess gravimetric adsorption isotherms for hydrogen at 298 K for IRMOF-1 (MOF-5). IRMOF-1 isotherm from data reported by Langmi et al. [125] and from values extracted from Yang et al. [124].

3. Discussion of the usable hydrogen storage capacities

3.1. Usable hydrogen storage capacities as a function of porosity, density and pore size

The GCMC simulations conducted at 298.15 K and 25 MPa produced results for usable capacities of different sets of MOFs: the two JLUs, the two Bi-based, the six P-based, the one Sb-based MOFs, the five In-based, the one Al-based, the 21 classical and the 23 rest-JLU MOFs. The results corresponding to JLU-MOF120 (Bi-based MOF), the two Bi-based, the six P-based, the one Sb-based MOFs, the 21 classical and the 23 rest-JLU MOFs are plotted in Figs. 3 and 5, illustrating how these capacities correlate with density, porosity, as well as both the largest and average pore size. Related outcomes have been obtained for JLU-MOF121 (In-based MOF), the five In-based, the one Al-based, the 21 classical and the 23 rest-JLU MOFs, and can be visualized in Figs. 4 and 6.

The usable capacities of both JLU-MOF120 and JLU-MOF121 decrease as the density of the material increases and increase as the porosity of the material increases, as can be seen in Figs. 3 and 4. There are some MOFs do not conform to these general trends. Additionally, it is worth noting that in Figs. 3 and 4, the gravimetric and volumetric capacities of JLU MOFs align with the overall trend observed in classical

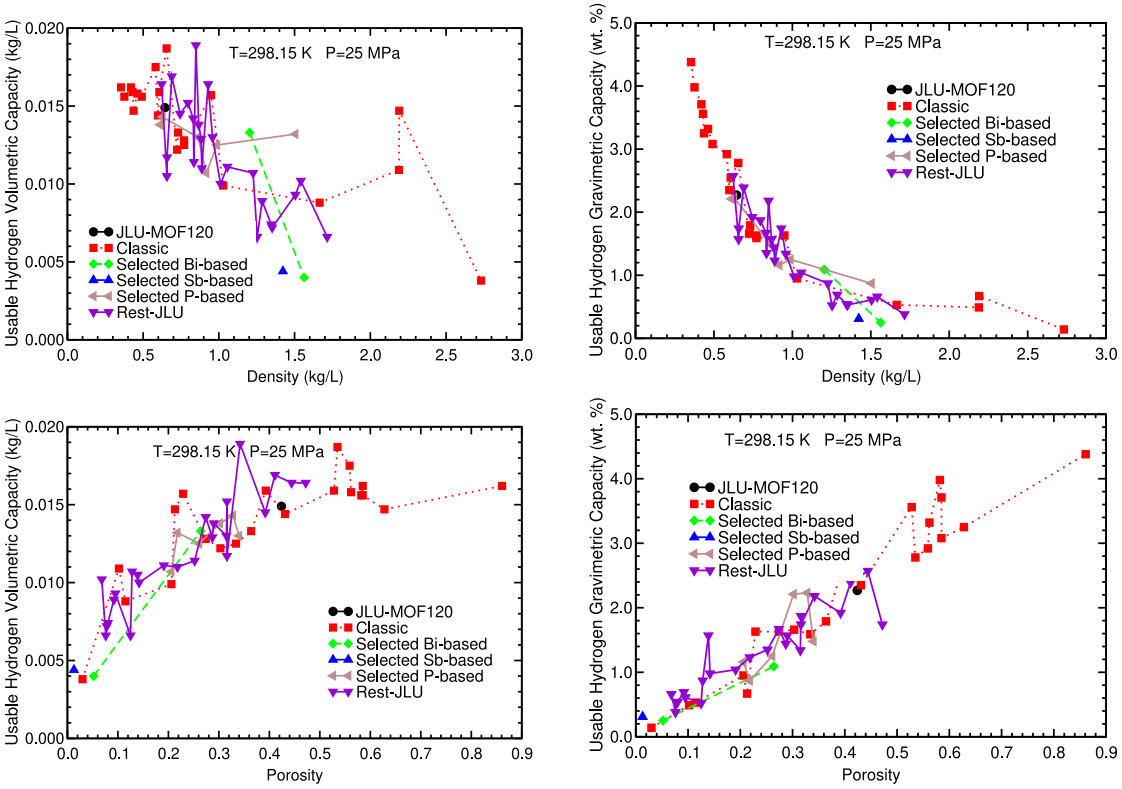

Fig. 3. Usable hydrogen gravimetric and volumetric capacity at 298.15 K and 25 MPa vs density and porosity for JLU-MOF120, Bi-based, P-based, Sb-based, classical and rest-JLU MOFs.

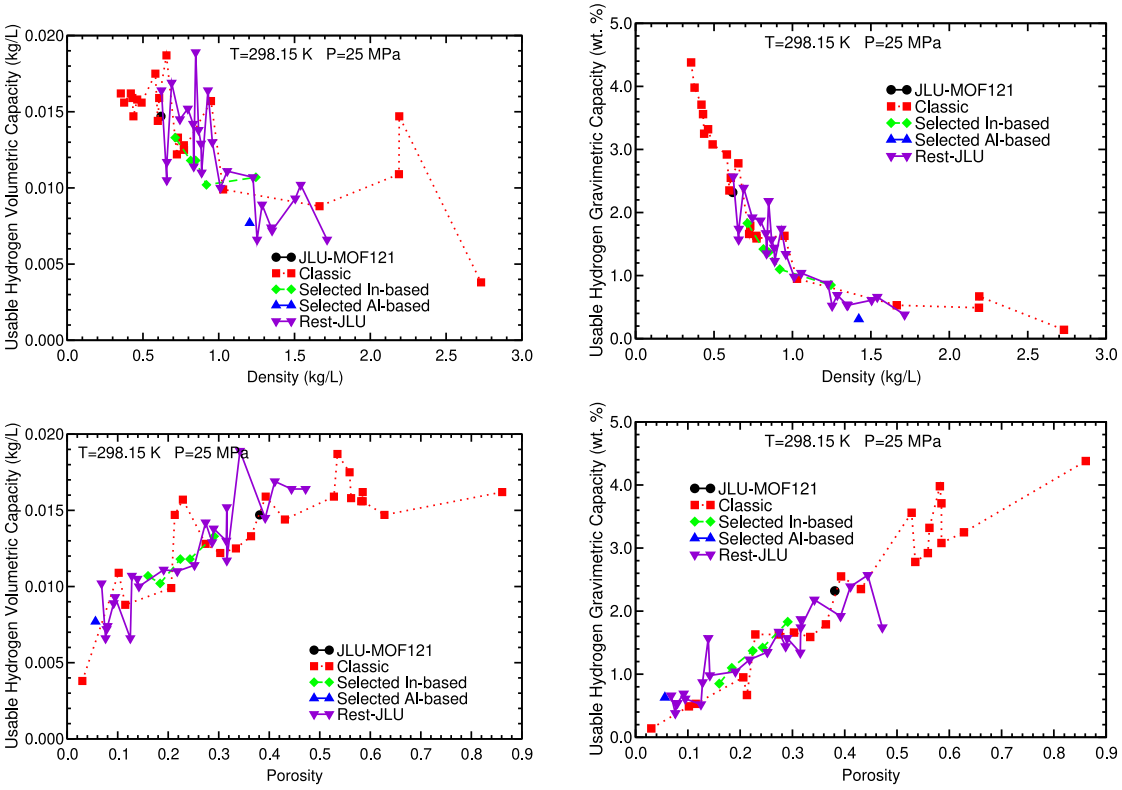

Fig. 4. Usable hydrogen gravimetric and volumetric capacity at 298.15 K and 25 MPa vs density and porosity for JLU-MOF121, In-based, Al-based, classical and rest-JLU MOFs.

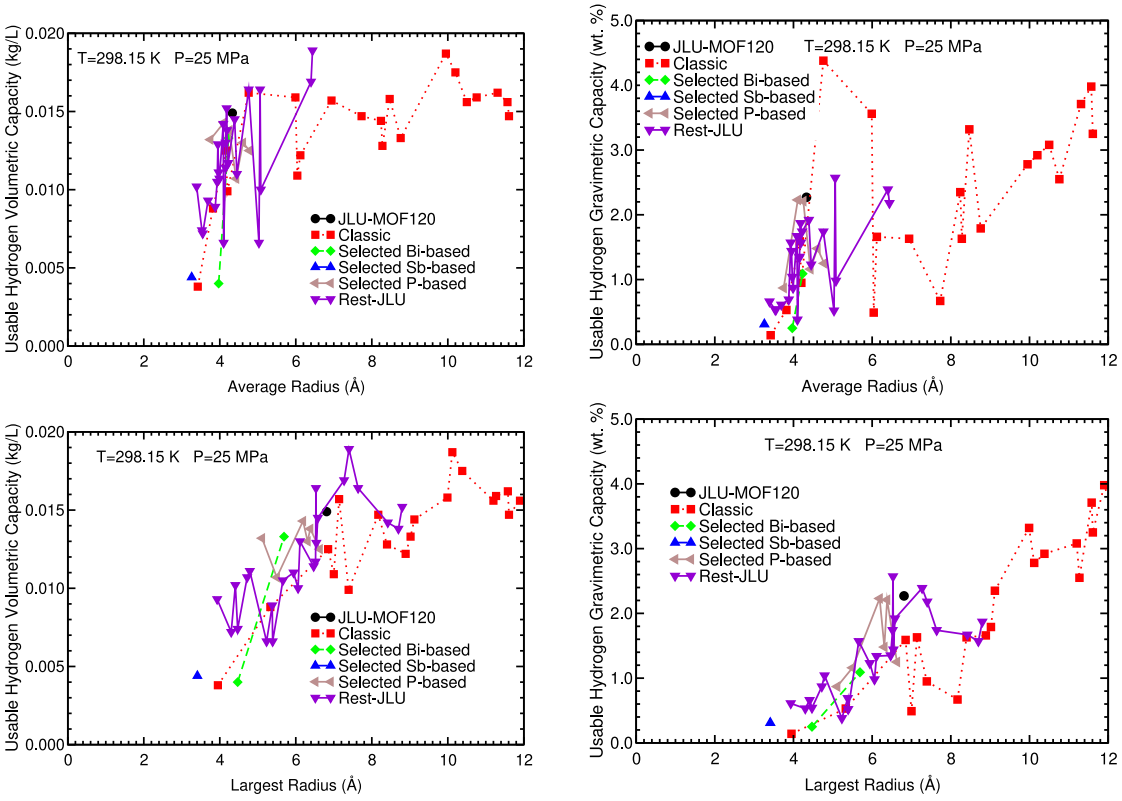

Fig. 5. Usable hydrogen gravimetric and volumetric capacity at 298.15 K and 25 MPa vs largest and average pore radius for JLU-MOF120, Bi-based, P-based, Sb-based, classical and rest-JLU MOFs.

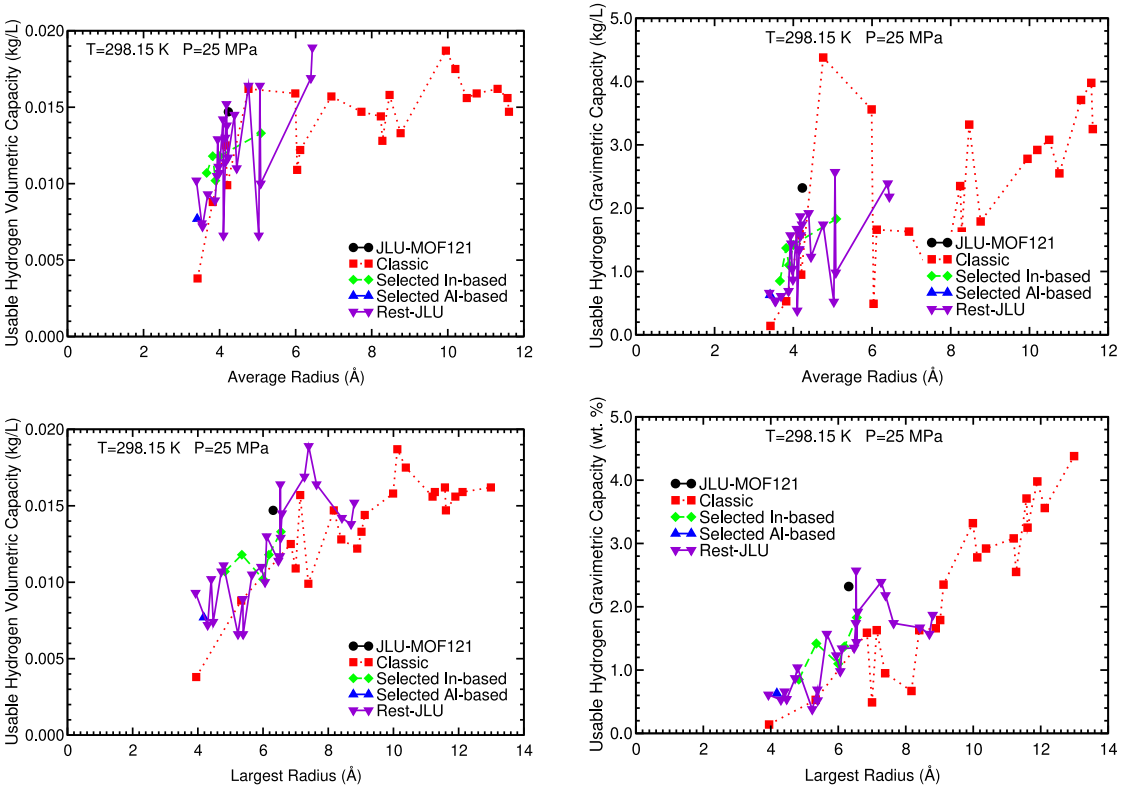

Fig. 6. Usable hydrogen gravimetric and volumetric capacity at 298.15 K and 25 MPa vs largest and average pore radius for JLU-MOF121, In-based, Al-based, classical and rest-JLU MOFs.

Table 6
Usable hydrogen volumetric (in kg/L) and gravimetric (in wt. %) capacities at 298.15 K and 25 MPa obtained in the present GCMC simulations, density ρ (in kg/L), porosity and largest R_l and average R_{av} pore radius (in Å) of the JLU MOFs, the selected Bi and In-related, the classical and the rest-JLU MOFs.

MOF	Ratio C/metal	Porosity	ρ	R_l	R_{av}	v_c	g_c
JLU-MOF120	C/Bi = 28.0	0.424	0.644	6.81	4.33	0.0149	2.27
JLU-MOF120-Sb	C/Sb = 28.0	0.421	0.562	6.81	4.33	0.0149	2.57
QOXQEC	C/P = 28.0	0.328	0.628	6.19	4.11	0.0143	2.23
FAGMAE	C/Sb = 30.0	0.013	1.423	3.41	3.26	0.0044	0.31
IZUKIZ	C/Bi = 27.0	0.264	1.203	5.69	4.23	0.0133	1.09
JLU-MOF121	C/In = 30.0	0.381	0.619	6.31	4.23	0.0147	2.32
JLU-MOF121-Ga	C/Ga = 30.0	0.378	0.574	6.31	4.23	0.0147	2.50
ROLRES	C/In = 28.0	0.291	0.713	6.55	5.09	0.0133	1.83
XEJTIR	C/Al = 28.0	0.056	1.204	4.18	3.41	0.0077	0.63
IRMOF-15	C/Zn = 12.0	0.861	0.354	12.99	4.76	0.0162	4.38
IRMOF-20	C/Zn = 7.5	0.535	0.655	10.12	9.95	0.0187	2.78
JLU-Liu30	C/Cu = 16.4	0.342	0.848	7.40	6.44	0.0189	2.18
JLU-Liu39	C/Cu = 7.6	0.444	0.622	6.53	5.06	0.0164	2.57

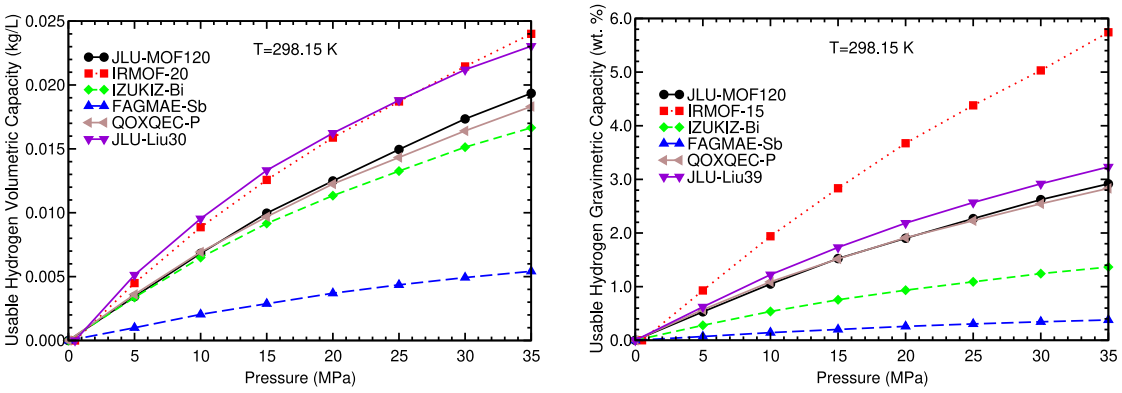

Fig. 7. Usable hydrogen volumetric and gravimetric capacities vs pressure at room temperature of the best P, Sb and Bi-related, classical and rest-JLU MOFs and JLU-MOF120.

and in rest-JLU MOFs. In the case of JLU-MOF120, its capacities also align with the trends observed in selected P-based MOFs concerning density and porosity. On the other hand, the gravimetric and volumetric capacities of JLU-MOF121 follow the trends established by the capacities of In-based MOFs vs density and porosity (see Fig. 4). This suggests the possibility of predicting the usable gravimetric capacity of a JLU material based on either its density or porosity.

The relationship between usable hydrogen storage capacities and both the largest and average pore radius is illustrated in Figs. 5 and 6 for JLU-MOF120 and JLU-MOF121, respectively. The usable gravimetric capacity demonstrates a linear increase as both, the largest and average pore radius, increase. It should be noted that, as a general tendency, an increase in pore radius leads to a decrease in material density, consequently resulting in an increase in gravimetric capacity. However, it is important to note that this trend is a rough approximation and might not be entirely precise.

Regarding the usable hydrogen volumetric capacity, an initial increase in the pore radius enhances the volumetric capacity. However, after a certain point, a saturation effect becomes evident, causing the volumetric capacity to rapidly approach a constant value with further increases in pore radius. The usable volumetric capacity can be roughly estimated using a function of the form $a - b/R$, where R represents either the largest or the average pore radius.

Classical, rest-JLU, P, Bi, Sb, In and Al-based MOFs with the highest gravimetric and volumetric capacities at room temperature and 25 MPa were chosen to compare with each of the JLUs in Table 6. For JLU-MOF120, the best P, Bi and Sb-based MOFs were chosen: QOXQEC (P-based) [132], IZUKIZ (Bi-based) [133] and FAGMAE (Sb-based MOF) [134]. For JLU-MOF121, the best In and Al-based MOFs were selected: ROLRES (In-based), which was reported as a gas storage and separation MOF [135], and XEJTIR (Al-based) [136]. Among the rest-JLU set, JLU-Liu30 [137] showcases the highest hydrogen volumetric capacity, while JLU-Liu39 [138] takes the lead in gravimetric capacity. The usable hydrogen storage capacities, densities, porosities and pore sizes for all these MOFs on Table 6 will be used to analyze and compare the storage capacities in the next subsections.

3.2. Usable hydrogen storage capacities as a function of pressure

The storage capacities of JLU-MOF120, its metal-related MOFs (P, Sb, and Bi-based), classical MOFs, and rest-JLU MOFs with the highest storage capacities at 25 MPa and 298.15 K are depicted against pressure in Fig. 7. IRMOF-20 and JLU-Liu30 exhibit the highest usable volumetric capacity across a pressure range of 0.5 to 35 MPa. JLU-MOF120 shows values closely resembling those of IRMOF-20 and JLU-Liu30, but they are approximately 21% lower than the capacities of IRMOF-20 and JLU-Liu30.

Notably, JLU-MOF120 achieved the highest value at 35 MPa, 0.019 kg/L which is about one half of the DOE target, 0.04 kg/L [8,15]. Furthermore, IZUKIZ and QOXQEC volumetric capacities are close to those of JLU-MOF120. QOXQEC has the same C/metal ratio as JLU-MOF120, but with P instead of Bi. On the other hand, IZUKIZ has the same metal, Bi, but with a slightly different C/Bi ratio. As a result, the similarities in terms of porosity, density, radius, and ratio between QOXQEC and JLU-MOF120 (see Table 6) result in comparable usable volumetric hydrogen isotherms (see left panel of Fig. 7). IZUKIZ and JLU-MOF120 exhibit different values for those structural properties and different capacities, suggesting that whether the metal is the same or not, the structural properties affect the volumetric capacity. On the other hand, despite FAGMAE has a lighter metal than Bi, Sb, it has a very high density and a very low porosity (see Table 6), resulting in

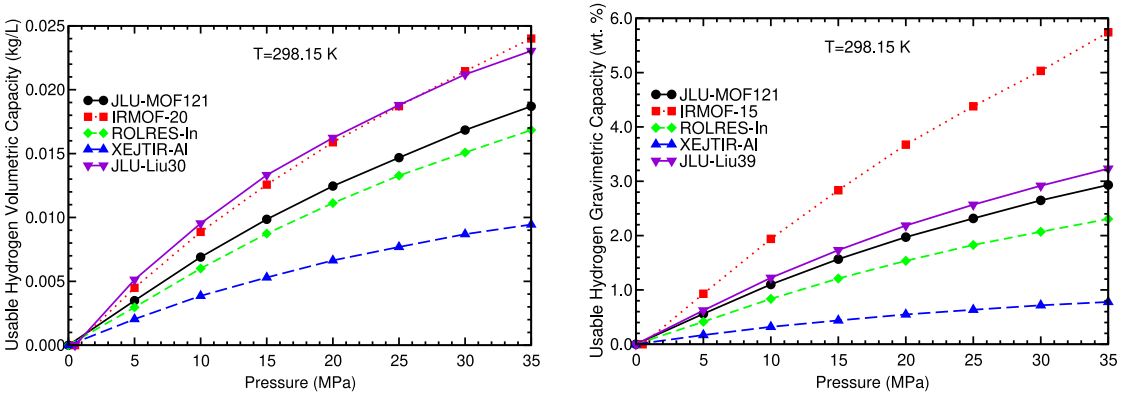

Fig. 8. Usable hydrogen volumetric and gravimetric capacities vs pressure at room temperature of the best Al and In-related, classical and rest-JLU MOFs and JLU-MOF121.

very low volumetric capacities, compared to the other MOFs, as can be noticed in left panel of Fig. 7.

As regards the usable gravimetric capacity of the MOFs considered, IRMOF-15 stood out with the highest gravimetric capacity at various pressures and room temperature and reaching the DOE target of 5.5 wt. % at approximately 35 MPa. JLU-MOF120 exhibits a similar increasing trend in usable hydrogen gravimetric capacity as pressure rises, reaching its peak at 35 MPa with a gravimetric capacity of 2.9 wt. %. However, this value is approximately 45% lower than the DOE gravimetric target. QOXQEC demonstrated usable gravimetric capacities comparable to those of JLU-MOF120 across all pressure levels, as can be noticed in the right panel of Fig. 7. Specifically, the gravimetric capacity of JLU-Liu39 was discovered to be only 13% higher than that of JLU-MOF120. In contrast, IZUKIZ displayed notably lower usable gravimetric capacities, roughly 50% lower than the JLU-MOF120 capacities, despite both MOFs are composed of Bi and have similar C/Bi ratios. JLU-MOF120, QOXQEC and IZUKIZ have similar C/metal ratios. These usable gravimetric capacity results are explained mainly by the different density: JLU-MOF120, JLU-Liu39 and QOXQEC have very similar densities, but the density of IZUKIZ is about two times larger (see Table 6), which explains that the IZUKIZ usable gravimetric capacities are about 45% lower. Additionally, FAGMAE exhibited the lowest gravimetric capacity among the MOFs considered, due to its lower porosity and larger density (see Table 6). This observation implies that having significantly different porosity and density directly impacts on the gravimetric storage capacity.

The capacities of the JLU-MOF121, of its metal related MOFs (Al and In-based) and the classical MOFs with the highest storage capacities at 25 MPa and 298.15 K are plotted as a function of the pressure in Fig. 8. The classic IRMOF-20 and the JLU-Liu30 have the highest usable volumetric capacity, also in this case. JLU-MOF121 exhibited values quite similar to those of JLU-MOF120, yielding the same conclusions as discussed above. JLU-MOF121 also reaches the highest usable volumetric capacity, 0.019 kg/L, at 35 MPa. Furthermore, ROLRES follows the same tendency as JLU-MOF121 with values of the usable volumetric capacity being only approximately 10% lower than those of the JLU-MOF121 (see the left panel of Fig. 8). On the other hand, XEJTIR exhibited volumetric capacities approximately 50% lower than those of JLU-MOF121. Consequently, the small differences between the ROLRES, the JLU-Liu39 and JLU-MOF121 usable hydrogen volumetric capacities might be attributed to their minor differences in terms of the structural magnitudes porosity, density, radii and C/In ratio (see Table 6). On the contrary, XEJTIR and JLU-MOF121 have also similar C/metal ratios, but they do not exhibit any commonalities in those structural magnitudes, specifically in the porosity and density (see Table 6), which resulted in markedly different volumetric storage capacities.

The classic IRMOF-15 has the largest usable gravimetric capacity (see the right panel of Fig. 8). JLU-MOF121 showed similar trend in the gravimetric storage capacity as JLU-MOF120 as a function of the pressure, reaching the same conclusions as those obtained for JLU-MOF120. ROLRES usable gravimetric capacities follows closely the JLU-MOF121 gravimetric capacities, but they are 23% lower. XEJTIR gravimetric capacities are very far from those of JLU-MOF121, about 73% lower. The similarities and differences in the porosity and density of JLU-MOF121, JLU-Liu39, ROLRES and XEJTIR (see Table 6) explain the similarities and differences of the gravimetric isotherms in the right panel of Fig. 8: The lower the porosity, the lower the gravimetric capacity and the lower the density, the larger the gravimetric capacity.

3.3. Usable hydrogen storage capacities of original JLUs and JLUs with metal change as a function of pressure

In order to dilucidate some insights into the impact of the metal component on the hydrogen adsorption, the metals in both JLU-MOFs were replaced with some metal in the same column of the periodic table. Specifically, antimony (Sb) replaced bismuth (Bi) in JLU-MOF120, resulting in JLU-MOF120-Sb, while gallium (Ga) replaced indium (In) in JLU-MOF121, leading to JLU-MOF121-Ga. The usable hydrogen storage capacities at 298.15 K for both original JLUs and their modified counterparts are graphically represented in Fig. 9 across a pressure range from 0.5 to 35 MPa.

The usable volumetric isotherms, as shown in Fig. 9, of the four JLU-MOFs are quite alike at 298.15 K and in a range from 0.5 to 35 MPa. The highest value is reached at 35 MPa and is about 0.019 kg/L. This is about the one half of the DOE target, 0.04 kg/L [8,15]. The original JLUs exhibit comparable usable gravimetric capacities to one another reaching about 2.9 wt. % at 35 MPa. The usable gravimetric capacities of the modified JLUs are also similar to each other and they achieve about 3.2 wt. % at 35 MPa. These two values are approximately the 53% and 58% of the DOE gravimetric target, 5.5 wt. MOFs, original and modified JLUs, respectively. JLU-MOF120-Sb and JLU-MOF121-Ga show slightly higher gravimetric capacities than their original counterparts. The modified JLUs have higher gravimetric capacities, because of their slightly lower densities, due to the replacement of the original metal atoms with lighter ones from the same column of the periodic table.

4. Discussion of the usable methane storage capacities

4.1. Usable methane storage capacities as a function of porosity, density and pore size of JLU MOFs

The methane storage capabilities of these MOFs were also investigated. The dependence between the usable methane storage capacities at 298.15 K and 25 MPa on the density, porosity and pore size of the MOFs is plotted in Figs. 10–13.

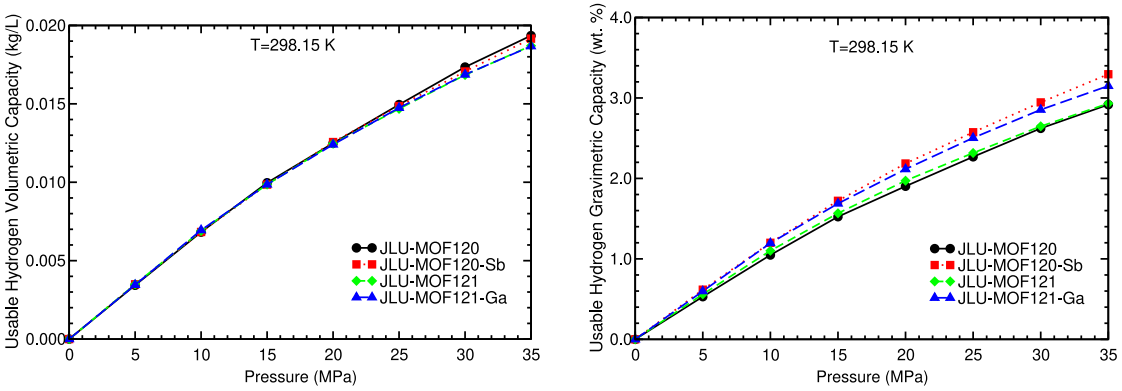

Fig. 9. Usable hydrogen volumetric and gravimetric capacities vs pressure of the original and modified JLUs at room temperature.

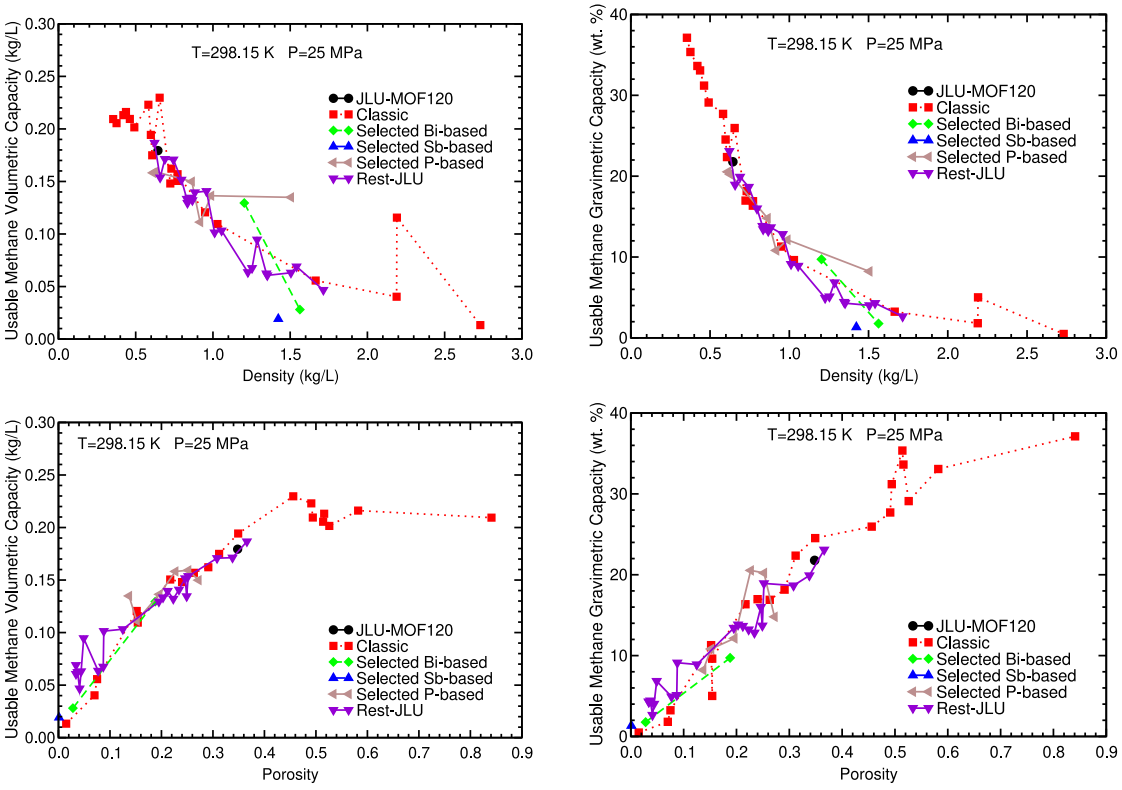

Fig. 10. Usable methane gravimetric and volumetric capacity at 298.15 K and 25 MPa vs density and porosity for JLU-MOF120, Bi-based, P-based, Sb-based MOFs, classical and rest-JLU MOFs.

The correlations between usable methane capacities and both porosity and density exhibit similarities to the correlations observed for hydrogen (see Figs. 10 and 11). Furthermore, it is noteworthy that in Figs. 3 and 4, the usable gravimetric capacities of JLU MOFs are close to the pattern established by the usable gravimetric capacities, as a function of the density, of classical MOFs, rest-JLU set and the metal-related sets for each JLU: Bi, P and Sb-based for JLU-MOF120, and Al and In-based for JLU-MOF121. This suggests that the usable methane gravimetric capacities of JLU MOFs can be predicted based on their densities. As for porosity, both JLUs, along with metal-related, classical and rest-JLU MOFs, generally experience an increase in usable methane storage capacities as porosity rises, mirroring the trends observed with hydrogen.

Figs. 12 and 13 illustrate the dependence of the usable methane storage capacities on the largest and average pore radius. These methane storage capacities exhibit the same relationship with these two radii as observed with hydrogen storage capacities. Similar to the case of hydrogen, an increase in pore radius corresponds to a decrease in density, leading to an augmentation in the usable gravimetric capacity and suggesting a tendency to follow a linear pattern. The usable volumetric capacity also experiences a rapid increase before reaching an asymptotic value as the largest or the average pore radii increase. The usable methane volumetric capacity can be roughly estimated using the function $a - b/R$, where R represents either the largest or the average pore radius.

As proceeded for the hydrogen capacities, the classical MOFs, the rest-JLU MOFs and the Bi and In-related MOFs with the highest usable methane gravimetric and volumetric capacities at 25 MPa and room temperature were chosen to compare with each JLU. The usable methane storage capacities, C/metal ratios, densities, porosities and pore radii of the MOFs obtained in the GCMC simulations at 298.15 K and 25 MPa are presented in Table 7. All the selected metal-related MOFs are the same as for hydrogen case, with the exception of QOXQIG, which is a P-based MOF and has the highest usable methane

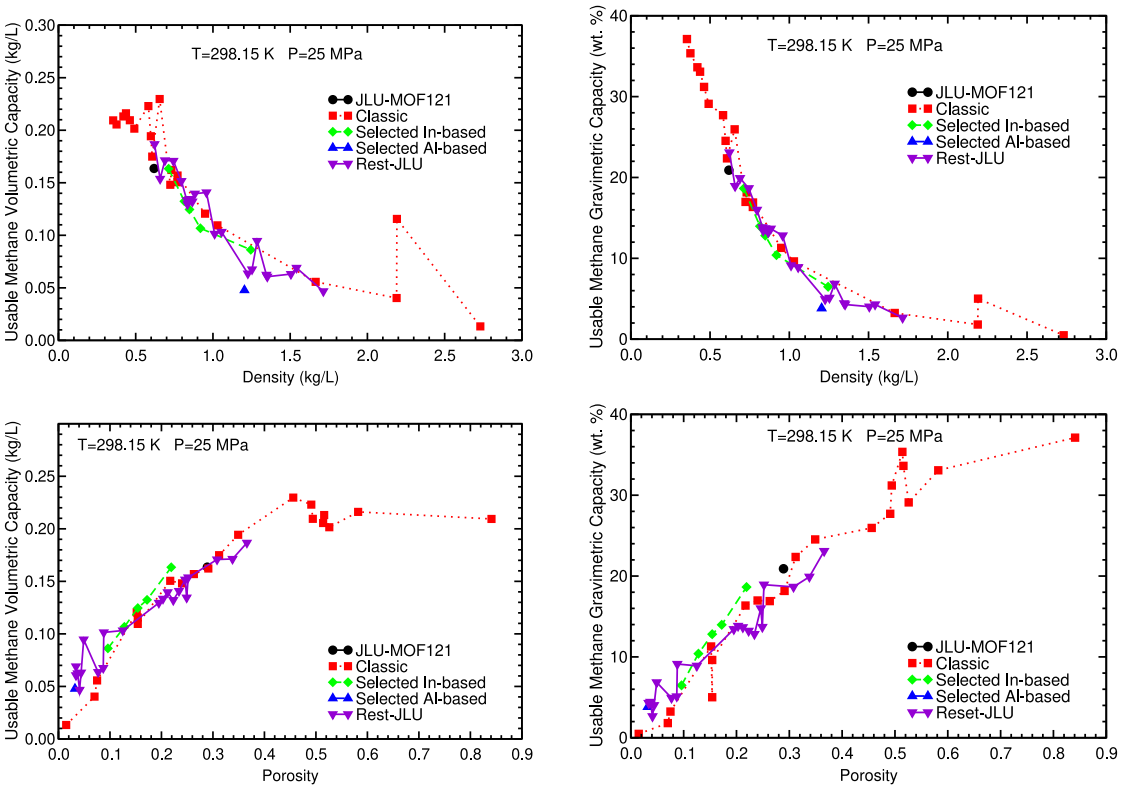

Fig. 11. Usable methane gravimetric and volumetric capacity at 298.15 K and 25 MPa vs density and porosity for JLU-MOF121, In-based, Al-based MOFs, classical and rest-JLU MOFs.

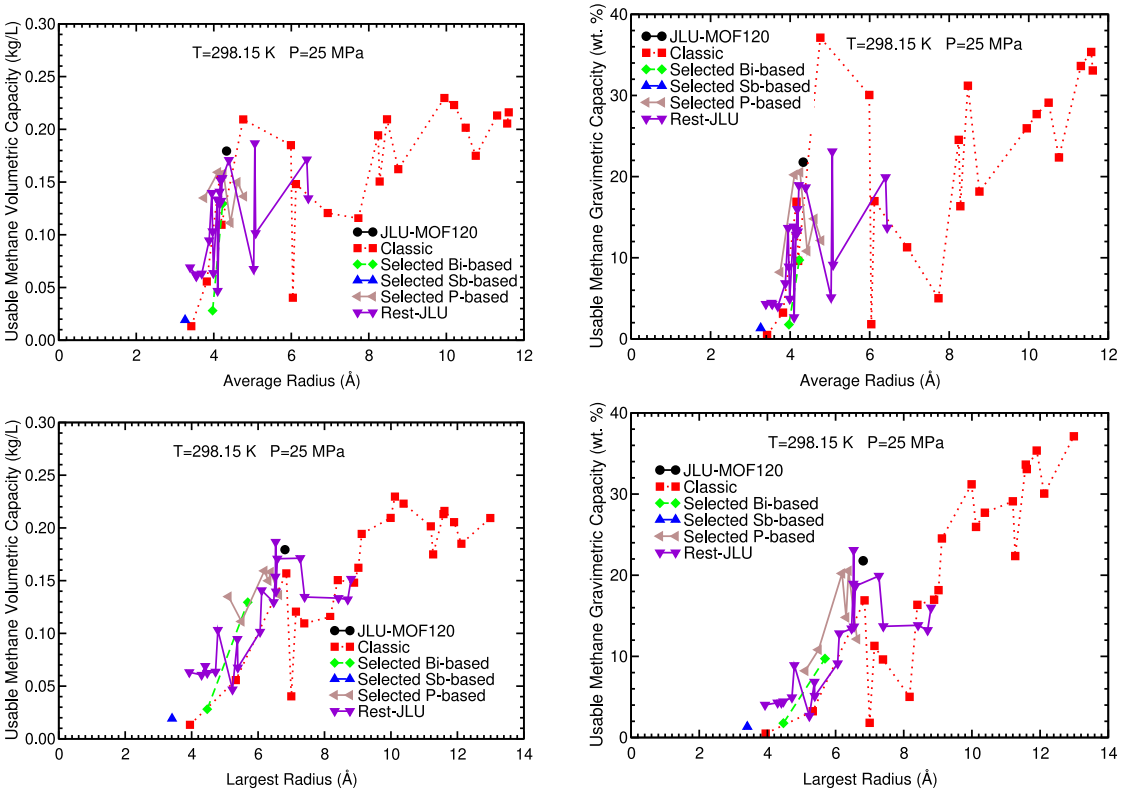

Fig. 12. Usable methane gravimetric and volumetric capacity at 298.15 K and 25 MPa vs largest and average pore radius for JLU-MOF120, Bi-based, P-based, Sb-based MOFs, classical and rest-JLU MOFs.

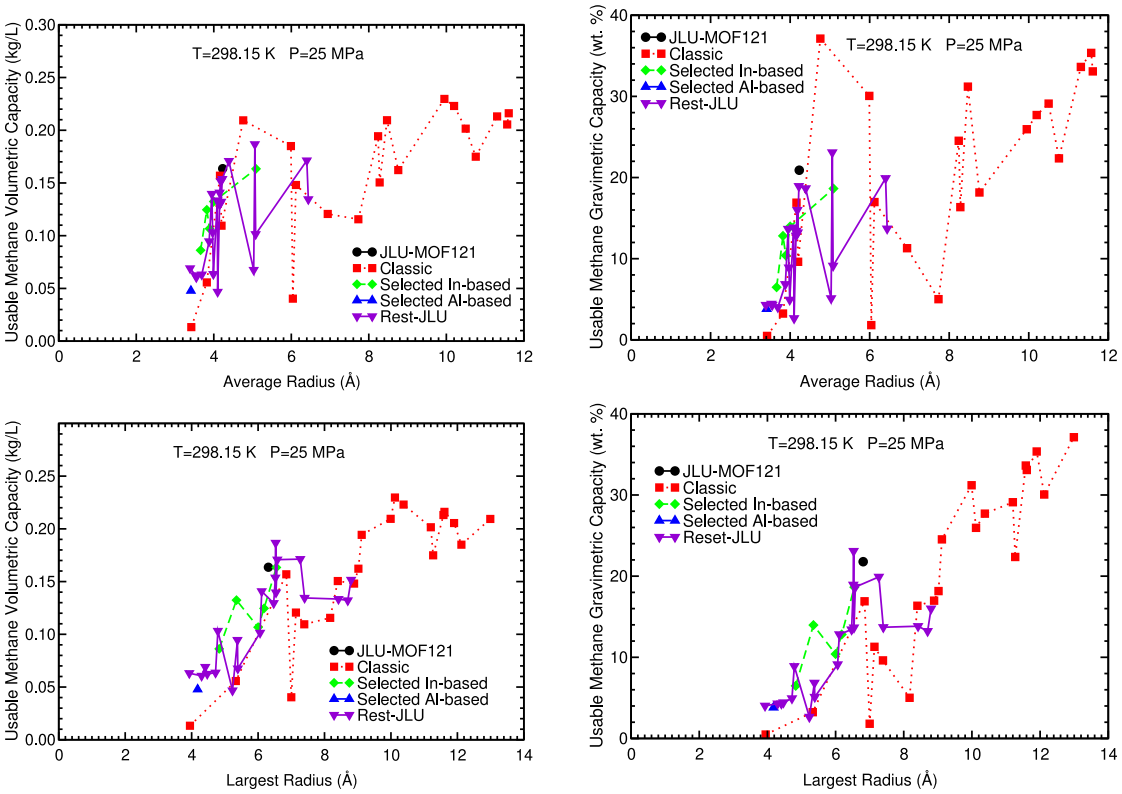

Fig. 13. Usable methane gravimetric and volumetric capacity at 298.15 K and 25 MPa vs largest and average pore radius for JLU-MOF121, In-based, Al-based MOFs, classical and rest-JLU MOFs.

Table 7
Usable methane volumetric (in kg/L) and gravimetric (in wt. %) capacities at 298.15 K and 25 MPa obtained in the present GCMC simulations, density ρ (in kg/L), porosity and largest R_l and average R_{av} pore radius (in Å) of the JLU MOFs, the selected Bi and In-related, the best classical and the best rest-JLU MOFs.

MOF	Ratio C/metal	Porosity	ρ	R_l	R_{av}	v_c	g_c
JLU-MOF120	C/Bi = 28.0	0.348	0.644	6.81	4.33	0.1794	21.78
JLU-MOF120-Sb	C/Sb = 28.0	0.345	0.562	6.81	4.33	0.1766	23.89
QOXQEC	C/P = 28.0	0.252	0.628	6.19	4.11	0.1593	20.22
QOXQIG	C/P = 29.0	0.227	0.628	6.19	4.11	0.1582	20.54
FAGMAE	C/Sb = 30.0	0.001	1.423	3.41	3.26	0.0192	1.33
IZUKIZ	C/Bi = 27.0	0.188	1.203	5.69	4.23	0.1295	9.72
JLU-MOF121	C/In = 30.0	0.289	0.619	6.31	4.23	0.1636	20.90
JLU-MOF121-Ga	C/Ga = 30.0	0.285	0.574	6.31	4.23	0.1613	21.94
ROLRES	C/In = 28.0	0.219	0.713	6.55	5.09	0.1634	18.64
XEJTIR	C/Al = 28.0	0.032	1.204	4.18	3.41	0.0478	3.82
IRMOF-15	C/Zn = 12.0	0.841	0.354	12.99	4.76	0.2094	37.12
IRMOF-20	C/Zn = 7.5	0.456	0.655	10.12	9.95	0.2297	25.95
JLU-Liu39	C/Cu = 7.6	0.366	0.622	6.53	5.06	0.1867	23.09

gravimetric capacity of all the P-based MOFs. In the context of rest-JLU set, JLU-Liu39 is the best for both gravimetric and volumetric methane storage capacity.

The usable methane gravimetric capacities of JLU-MOF120 and JLU-MOF121 are 22 and 21 wt. %, respectively. Their volumetric capacities, measured at room temperature and 25 MPa, stand at 0.18 and 0.16 kg/L, respectively. When comparing the usable methane storage capacities at 298.15 K and 25 MPa, it becomes evident that the usable methane volumetric capacities of JLUs are notably high. They exceed those of selected metal-related MOFs, but do not reach the highest volumetric and gravimetric capacities achieved by the best classical MOFs, IRMOF-20 and IRMOF-15 and the best rest-JLU MOF, JLU-Liu39 (see Table 7).

4.2. Usable methane storage capacities as a function of pressure

As previously proceeded, GCMC simulations were conducted to determine the usable methane storage capacities of JLU MOFs, the best metal-related MOFs, the best classical MOFs and the best rest-JLU MOFs at 298.15 K and across a range of pressures from 0.5 to 35 MPa. The results of these simulations are depicted in Figs. 14 and 15. Only IRMOF-20 comes close the usable methane volumetric DOE target, 0.25 kg/L [22–24] at 298.15 K and 35 MPa. The JLU-MOF120 volumetric capacity isotherm exhibited a shape closely resembling that of the IRMOF-20 volumetric capacity isotherm, but approximately 20% lower and reaching 0.19 kg/L at 35 MPa and 298.15 K. This is only 24% lower than the DOE volumetric goal [22–24]. The volumetric capacities of both JLU-MOF120 and JLU-Liu39 display a notable resemblance, as

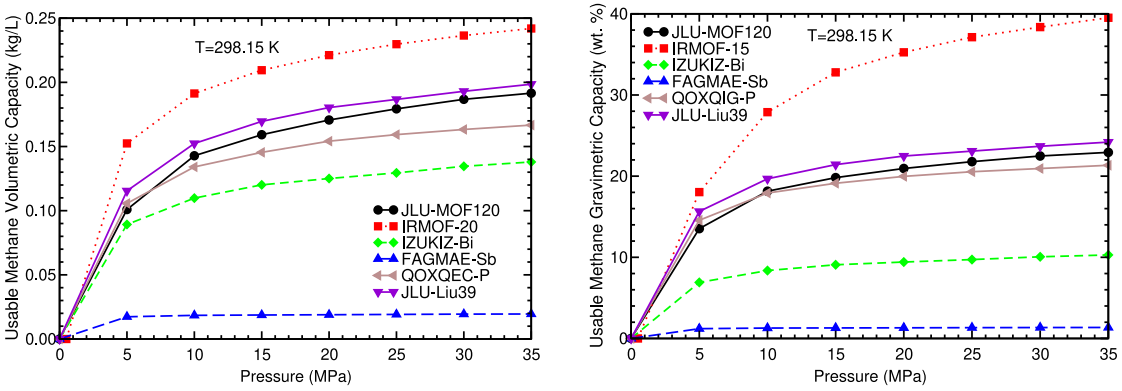

Fig. 14. Usable methane volumetric and gravimetric capacities vs pressure at room temperature of some selected Bi-related MOFs, the best rest-JLU MOF (JLU-Liu39) and JLU-MOF120.

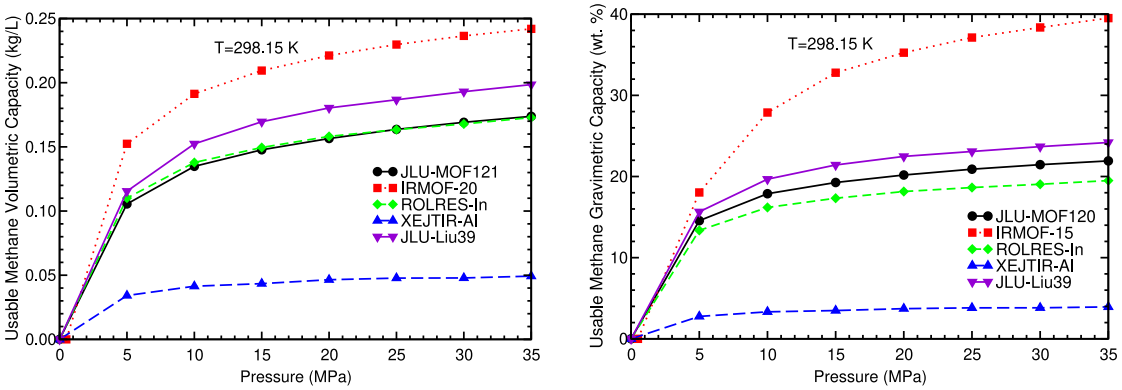

Fig. 15. Usable methane volumetric and gravimetric capacities vs pressure at room temperature of some selected In-related MOFs, the best rest-JLU MOF (JLU-Liu39) and JLU-MOF121.

their curves closely mirror each other. Notably, the volumetric values for JLU-MOF120 are slightly lower, approximately 4%, than those observed for JLU-Liu39. In contrast with hydrogen case, the isotherms of JLU-MOF120, IZUKIZ and QOXQEC are a little far from each other. On the other hand, FAGMAE contains Sb, a lighter metal than Bi, but it has a very high density and a very low porosity, resulting in very low volumetric capacities.

For usable methane gravimetric capacity, only IRMOF-15 manages to meet the DOE target, 33.3 wt. %, [22–24] at 298.15 K and 15 MPa. JLU-MOF120 exhibits a similar upward trend in usable methane gravimetric capacity as pressure rises, reaching its peak at 35 MPa with a gravimetric capacity of 23 wt. %. This achievement represents approximately 69% of the DOE target. Interestingly, QOXQIG and JLU-Liu39 MOFs demonstrate methane gravimetric capacities comparable to those of JLU-MOF120 across all pressure levels. Conversely, IZUKIZ displays notably lower gravimetric capacities, more than 50% lower than JLU-MOF120, despite both MOFs being composed of Bi. FAGMAE usable gravimetric capacities are very low. Since JLU-MOF120, JLU-Liu39 and QOXQIG have similar densities, and the densities of IZUKIZ and FAGMAE are much larger (see Table 7), these results suggests that the usable gravimetric capacity might not be influenced by the metal, but rather by the density and porosity.

JLU-MOF121 reaches its peak volumetric value, 0.17 kg/L, at 35 MPa. These volumetric capacities are 29% lower than those of IRMOF-20, 11% lower than those of JLU-Liu39 and 32% lower than the DOE volumetric target. Furthermore, ROLRES demonstrates a closely aligned trend with JLU-MOF121 with usable volumetric capacity almost overlapping those of the JLU-MOF121. On the other hand, XEJTIR followed a similar trend, but presented volumetric capacities approximately 70% lower than those of JLU-MOF121. Consequently, the small variations in methane volumetric values between ROLRES and JLU-MOF121 might be attributed to their minor porosity, density, radii and C/In ratio differences (see Table 7). The structural parameters of XEJTIR and JLU-MOF121 are different, except for a similar C/metal ratio. These differences result in markedly different volumetric storage capacities.

IRMOF-15 boasts the largest usable methane gravimetric capacity. JLU-MOF121 showed similar trend in the gravimetric storage capacity as JLU-MOF120 as a function of the pressure, reaching the same conclusions as those obtained for JLU-MOF120. ROLRES gravimetric capacities follow close the JLU-MOF121 gravimetric capacities, but about 10% lower. Gravimetric capacity values of JLU-Liu39 are only 5% above from those of JLU-MOF121. These gravimetric results can be explained with the densities: JLU-MOF121, JLU-Liu39 and ROLRES have similar densities and porosities and hence, similar gravimetric capacities, while XEJTIR has a higher density and lower porosity and hence, lower gravimetric capacities. As expected, the disparities in porosity and density result in markedly different gravimetric storage capacities.

4.3. Usable methane storage capacities of original JLUs and JLUs with metal change as a function of pressure

As proceeded in Section 3.3, to find out how the metal influences in the methane gas adsorption, the metals of both JLUs have been changed. The usable methane storage capacities at 298.15 K of the original and modified JLUs are plotted in Fig. 16 as a function of the pressure between 0.5 and 35 MPa.

The two original JLUs have comparable usable gravimetric capacities and the modified JLUs exhibited higher usable gravimetric capacities compared to the original JLUs. The gravimetric capacities of the four JLUs are approximately 25%–34% lower than the DOE gravimetric target, 33.33 wt. % [22]. They share similarities in terms

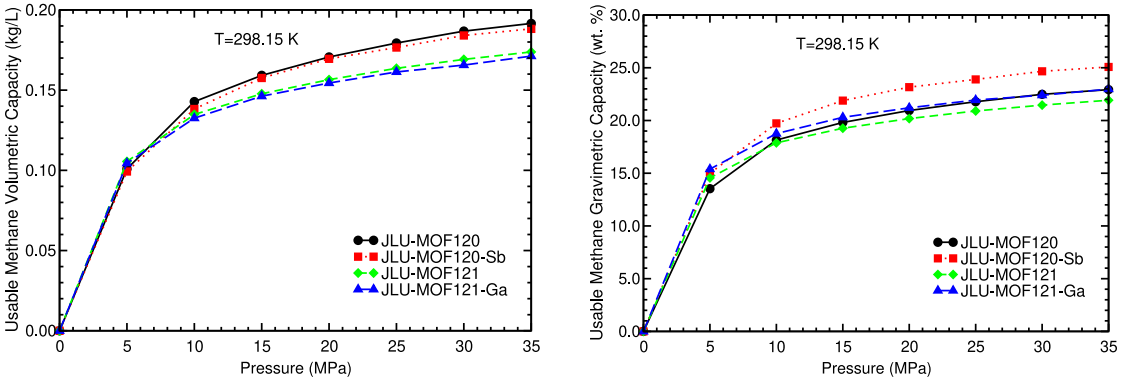

Fig. 16. Usable methane volumetric and gravimetric capacities vs pressure of the two JLUs and the two modified JLUs at room temperature.

of densities, porosities and radii. The gravimetric capacities of the JLU-MOF120-Sb and JLU-MOF121-Ga are higher than the gravimetric capacities of their counterparts, because antimony (Sb) is lighter than bismuth (B), and gallium (Ga) is lighter than indium (In), which implies that the density of the modified JLUs is smaller, as reflected in Table 7.

The usable methane volumetric capacities have been depicted as a function of pressure, ranging from 0.5 to 35 MPa at 298.15 K in Fig. 16. The volumetric capacities of the two original JLUs exhibit similar trends, yet the volumetric capacities of JLU-MOF120 are 11% higher than those of JLU-MOF121, reaching 0.19 kg/L and 0.17 kg/L, respectively, at 35 MPa. These capacities are approximately 24%–32% lower than the DOE volumetric target [22–24]. The volumetric capacities of the modified JLUs are very close and slightly smaller than the volumetric capacities of the original JLUs, which means that changing the metal atom does not lead to improved volumetric capacities.

5. Conclusions

GCMC simulations of the usable hydrogen and methane storage capacities at room temperature and pressures between 0.5 and 35 MPa of two JLU MOFs, JLU-MOF120 (Bi-based) and JLU-MOF121 (In-based), recently synthesized by a group of the Jilin University [93] have been carried out and analyzed. According to the present GCMC simulations, the two novel JLU MOFs have similar storage capacities and show high usable hydrogen and methane storage capacities at room temperature and pressures of 25–35 MPa, comparable to the capacities of the best classical MOFs and the best rest-JLU MOFs and larger than the capacities of MOFs based on Bi, In, P, Sb and Al. The best classical MOFs and the best rest-JLU MOFs still have larger usable hydrogen and methane volumetric and gravimetric capacities than the two JLUs studied. Specifically, the usable hydrogen gravimetric and volumetric storage capacities of the JLU MOFs, at 298.15 K and 25 MPa are about 2.3 wt. % and 0.015 kg/L, respectively. The usable methane storage, both gravimetric and volumetric capacities, of the JLUs at room temperature and 25 MPa are situated in the range of 20–22 wt. % and 0.16–0.18 kg/L, respectively.

The dependence of the usable hydrogen and methane storage capacities of the examined MOFs, including classical, rest-JLU, metal-related, and the two newly introduced JLU MOFs, on the porosity, density and the pore radius has been also studied. The results indicate a general trend where these capacities do not depend on the type of metal atom. Additionally, they exhibit an inverse relationship with density and a direct relationship with porosity and pore radius. The high storage capacities of the two recently developed JLU MOFs can be attributed to their substantial porosity, low density, and relatively wide pores. It is worth noticing that the present results are predictions of the storage capacities of real materials, the two JLU MOFs, and that these predictions could be useful for experimental researchers.

Declaration of competing interest

The authors declare that they have no known competing financial interests or personal relationships that could have appeared to influence the work reported in this paper.

Acknowledgments

This work has been funded by the MICINN research project from Spain (Grant PGC2018-093745-B-I00), the Junta de Castilla y León (Grant VA124G18), and the University of Valladolid, Spain. The authors gratefully acknowledge the financial support provided by these institutions, which made this research possible. The authors would also like to express their appreciation for the use of the computer facilities at the Centro de Procesado de Datos - Parque Científico of the University of Valladolid.

References

[1] What is energy? Sources of energy. 2023, https://www.eia.gov/energyexplained/what-is-energy/sources-of-energy.php. [Accessed 18 December 2023].
[2] Zhang L, Jia C, Bai F, Wang W, An S, Zhao K, et al. Fuel 2024;355:129455.
[3] Chakraborty S, Dash SK, Elavarasan RM, Kaur A, Elangovan D, Meraj ST, et al. Front Energy Res 2022;10:893475.
[4] Schlichtenmayer M, Hirscher M. Appl Phys A 2016;122:379.
[5] Jena P. J Phys Chem Lett 2011;2(3):206–11.
[6] Net Zero Emissions by 2050 Scenario (NZE). 2022, https://www.iea.org/reports/global-energy-and-climate-model/net-zero-emissions-by-2050-scenario-nze. [Accessed 22 December 2023].
[7] The long-term strategy of the United States, pathways to net-zero greenhouse gas emissions by 2050. 2021, https://unfccc.int/sites/default/files/resource/US-LongTermStrategy-2021.pdf. [Accessed 22 December 2023].
[8] Office of Energy Efficiency & Renewable Energy, Fuel Cell Technologies Office. DOE technical targets for onboard hydrogen storage for light-duty vehicles. 2018, https://www.energy.gov/eere/fuelcells/doe-technical-targets-onboard-hydrogen-storage-light-duty-vehicles. [Accessed 22 December 2023].
[9] Chu C, Wu K, Luo B, Cao Q, Zhang H. Carbon Resour Convers 2023;6(4):334–51.
[10] Broom DP, Webb CJ, Webb KE, Parilla PA, Gennett T, Brown CM, et al. Appl Phys A 2021;122:151.
[11] Breeze P. Power system energy storage technologies. London: Elsevier; 2018, p. 69–77.
[12] Hwang HT, Varma A. Curr Opin Chem Eng 2014;5:42–8.
[13] Ding F, Yakobson BI. Front Phys 2011;6:142–50.
[14] Assoualaye G, Tom A, Djongyang N. SN Appl Sci 2020;2:1815.
[15] Allendorf MD, Hulvey Z, Gennett T, Ahmed A, Autrey T, Camp J, et al. Energy Environ Sci 2018;11:2784–812.
[16] Sherburne M. Natural gas could bridge gap from gasoline to electric vehicles, thanks to metal-organic frameworks. 2022, https://news.umich.edu/natural-gas-could-bridge-gap-from-gasoline-to-electric-vehicles-thanks-to-metal-organic-frameworks. [Accessed 18 December 2023].
[17] CO_2 emission performance standards for cars and vans. 2023, https://climate.ec.europa.eu/eu-action/transport/road-transport-reducing-co2-emissions-vehicles/co2-emission-performance-standards-cars-and-vans_en. [Accessed 18 December 2023].

[18] Hren R, Vujanović A, Van Fan Y, Klemeš JJ, Krajnc D, Čuček L. Renew Sustain Energy Rev 2023;173:113113.
[19] Ogden J, Jaffe AM, Scheitrum D, McDonald Z, Miller M. Energy Policy 2018;115:317–29.
[20] Beckner M, Dailly A. Appl Energy 2015;149:69–74.
[21] Yabing H, Zhou W, Guodong Q, Chen B. Chem Soc Rev 2014;45:5657–78.
[22] Advanced Research Projects Agency - Energy, DOE. Methane opportunities for vehicular energy (MOVE) program overview. 2012, http://arpa-e.energy.gov/sites/default/files/documents/files/MOVE_ProgramOverview.pdf. [Accessed 3 January 2024].
[23] Advanced Research Projects Agency - Energy, DOE. Methane opportunities for vehicular energy (MOVE). 2012, https://arpa-e.energy.gov/technologies/programs/move. [Accessed 3 January 2024].
[24] International Organization for Standardization. ISO 15403-1:2006(en) natural gas — Natural gas for use as a compressed fuel for vehicles — Part 1: Designation of the quality. 2006, https://www.iso.org/obp/ui/#iso:std:iso:15403:-1:ed-1:v1:en. [Accessed 18 December 2023].
[25] Office of Energy Efficiency & Renewable Energy, Hydrogen and Fuel Cell Technologies Office. High-pressure hydrogen tank testing. 2022, https://www.energy.gov/eere/fuelcells/high-pressure-hydrogen-tank-testing. [Accessed 18 December 2023].
[26] Verma SK, Bhatnagar A, Shukla V, Soni PK, Pandey AP, Yadav TP, et al. Int J Hydrogen Energy 2020;45(38):19516–30.
[27] Singh S, Bhatnagar A, Shukla V, Vishwakarma AK, Soni PK, Verma SK, et al. Int J Hydrogen Energy 2020;45(1):774–86.
[28] Shukla V, Bhatnagar A, Verma SK, Pandey AP, Vishwakarma AK, Srivastava P, et al. Mater Adv 2021;2:4277–90.
[29] Bhatnagar A, Pandey AP, Hudson MSL, Soni PK, Verma SK, Shukla V, et al. Int J Energy Res 2021;45:6285–92.
[30] Pandey AP, Bhatnagar A, Shukla V, Soni PK, Singh S, Verma SK, et al. Int J Hydrogen Energy 2020;45(55):30818–27.
[31] He T, Pachfule P, Wu H, Xu Q, Chen P. Nat Rev Mater 2016;1:16059.
[32] Lu X, Tang Y, Yang G, Wang Y-Y. CrystEngComm 2023;25:896–908.
[33] Wu X, Wang Y, Cai Z, Zhao D, Cai W. Chem Eng Sci 2020;226:115837.
[34] Guo J, Morris JR, Ihm Y, Contescu CI, Gallego NC, Duscher G, et al. Small 2012;8:3283–8.
[35] Cabria I, Suárez-García F, Mazadiego LF, Ortega MF. 21st century nanoscience – A handbook: Low-dimensional materials and morphologies, volume 4. Boca Raton: CRC Press; 2020, p. 1–14.
[36] Pandey SK, Verma SK, Bhatnagar A, Yadav TP. Int J Energy Res 2022;46:17602–15.
[37] Verma SK, Shaz MA, Yadav TP. Int J Hydrogen Energy 2023;48:21383–94.
[38] Verma SK, Bhatnagar A, Shaz MA, Yadav TP. Int J Hydrogen Energy 2023;48:9762–75.
[39] Verma SK, Shaz MA, Yadav TP. Energy Storage 2022;4:e333.
[40] Yousaf M, Ahmad M, Zhao Z-P, Ishaq T, Mahmood N. Materials for hydrogen production, conversion, and storage. John Wiley & Sons, Ltd; 2023, p. 655–80.
[41] Granja-DelRío A, Cabria I. Int J Hydrogen Energy 2024;50:685–96.
[42] Cabria I. Int J Hydrogen Energy 2024;50:160–77.
[43] Caviedes D, Cabria I. Int J Hydrogen Energy 2022;47:11916–28.
[44] Karki S, Chakraborty SN. Microporous Mesoporous Mater 2021;317:110970.
[45] Cabria I, Lebon A, Torres M, Gallego L, Vega A. Appl Surf Sci 2021;562:150019.
[46] Kessler C, Eller J, Gross J, Hansen N. Microporous Mesoporous Mater 2021;324:111263.
[47] Cabria I. Int J Hydrogen Energy 2020;45:5697–709.
[48] Xu W, Chen Y, Song M, Liu X, Zhao Y, Zhang M, Zhang C. J Phys Chem C 2020;124(15):8110–8.
[49] Li B, Wen H-M, Zhou W, Xu JQ, Chen B. Chem 2016;1:557–80.
[50] Cheng Y-H, Zhang C-Y, Ren J, Tong K-Y. Front Phys 2016;11(5):113101.
[51] Blanco AAG, Vallone AF, Korili SA, Gil A, Sapag K. Microporous Mesoporous Mater 2016;224:323–31.
[52] Hassani A, Mosavian HMT, Ahmadpour A, Farhadian N. J Chem Phys 2015;142(23):234704.
[53] Chouhan RK, Ulman K, Narasimhan S. J Chem Phys 2015;143(4):044704.
[54] Peng Y, Krungleviciute V, Eryazici I, Hupp JT, Farha OK, Yildirim T. J Am Chem Soc 2013;135(32):11887–94.
[55] Zhou X, Zhou J, Sun Q. Front Phys 2011;6:220–3.
[56] Li S, Zhao H-M, Jena P. Front Phys 2011;6:204–8.
[57] Li J, Furuta T, Goto H, Ohashi T, Fujiwara Y, Yip S. J Chem Phys 2003;119(4):2376–85.
[58] Donà L, Brandenburg JG, Civalleri B. J Chem Phys 2022;156(9):094706.
[59] Fanourgakis GS, Gkagkas K, Froudakis G. J Chem Phys 2022;156(5):054103.
[60] Jose R, Bangar G, Pal S, Rajaraman G. J Chem Sci 2023;135:19.
[61] Nath K, Ahmed A, Siegel DJ, Matzger AJ. Angew Chem Int Edn 2022;61(25):e202203575.
[62] Zhao D, Wang X, Yue L, He Y, Chen B. Chem Commun 2022;58:11059–78.
[63] Forrest KA, Verma G, Ye Y, Ren J, Ma S, Pham T, et al. Chem Phys Rev 2022;3(2):021308.
[64] Li A. J Phys: Conf Ser 2022;2403(1):012022.
[65] Suresh K, Aulakh D, Purewal J, Siegel DJ, Veenstra M, Matzger AJ. J Am Chem Soc 2021;143(28):10727–34.
[66] Zhang X, Lin R-B, Wang J, Wang B, Liang B, Yildirim T, et al. Adv Mater 2020;32(17):1907995.
[67] Broom DP, Webb CJ, Fanourgakis GS, Froudakis GE, Trikalitis PN, Hirscher M. Int J Hydrogen Energy 2019;44(15):7768–79.
[68] Kim J, Yeo S, Jeon J-D, Kwak S-Y. Microporous Mesoporous Mater 2015;202:8–15.
[69] Rydén J, Öberg S, Heggie M, Rayson M, Briddon P. Microporous Mesoporous Mater 2013;165:205–9.
[70] Hirscher M, Panella B, Schmitz B. Microporous Mesoporous Mater 2010;129(3):335–9.
[71] Fei S, Alizadeh A, Hsu W-L, Delaunay J-J, Daiguji H. J Phys Chem C 2021;125(48):26755–69.
[72] Hu X, Wang J, Li S, Hu X, Ye R, Zhou L, et al. RSC Adv 2023;13:14980–90.
[73] Park J, Adhikary A, Moon HR. Coord Chem Rev 2023;497:215402.
[74] Sengupta D, Melix P, Bose S, Duncan J, Wang X, Mian MR, et al. J Am Chem Soc 2023;145(37):20492–502.
[75] Zhang X, Zheng Q-R, He H-Z. Int J Hydrogen Energy 2023 [in press].
[76] Li F-G, Liu C, Yuan D, Dai F, Wang R, Wang Z, et al. CCS Chem 2022;4(3):832–7.
[77] Peedikakkal AMP, Aljundi IH. Appl Sci 2021;11(24):11687.
[78] Mason JA, Oktawiec J, Taylor MK, Hudson MR, Rodriguez J, Bachman JE, et al. Nature 2015;527:357–61.
[79] Zhang G, Liang Y, Cui G, Dou B, Lu W, Yang Q, et al. Energy Rep 2023;9:2852–60.
[80] Yu Y, Shang M, Kong L, Wang L, Sun T. Chemosphere 2023;321:138160.
[81] Singh M, Shukla A, Chakraborty B. Sustain Energy Fuels 2023;7:996–1010.
[82] Yeh C-H, Khan AH, Miyazak T, Jiang J-C. Phys Chem Chem Phys 2021;23:12270–9.
[83] Li D-Z, Chen L, Liu G, Yuan Z-Y, Li B-F, Zhang X, et al. New Carbon Mater 2021;36(3):468–96.
[84] Rosen AS, Notestein JM, Snurr RQ. ACS Catal 2019;9(4):3576–87.
[85] Tsivion E, Mason JA, Gonzalez MI, Long JR, Head-Gordon M. Chem Sci 2016;7:4503–18.
[86] Sur M, Dornfeld M, Ganz E. J Chem Phys 2009;131(17):174703.
[87] Samanta A, Furuta T, Li J. J Chem Phys 2006;125(8):084714.
[88] Sagara T, Ortony J, Ganz E. J Chem Phys 2005;123(21):214707.
[89] Sagara T, Klassen J, Ganz E. J Chem Phys 2004;121(24):12543–7.
[90] Ahmed A, Seth S, Purewal J, Wong-Foy AG, Veenstra M, Matzger AJ, et al. Nature Commun 2019;10:1568.
[91] Fu J, Tian Y, Wu J. Adsorption 2015;21:499–507.
[92] Basdogan Y, Keskin S. CrystEngComm 2015;17:261–75.
[93] Zhu Y, Cai J, Xu L, Li G, Liu Y. Inorg Chem 2022;61(28):10957–64.
[94] Metropolis N. Los Alamos Sci 1987;15:125–30.
[95] Soave G. Chem Eng Sci 1972;27:1197–203.
[96] Zhou L, Zhou Y. Int J Hydrogen Energy 2001;26:597–601.
[97] Xu X-H, Duan Y-Y, Yang Z. Ind Eng Chem Res 2012;51:6580–5.
[98] Lennard-Jones JE. Proc R Soc (London) A 1924;106:463–77.
[99] Berthelot D. C. R. Hebd. Seances Acad. Sci. 1898;126:1703.
[100] Good RJ, Hope CJ. J Chem Phys 1970;53:540–3.
[101] Rzepka M, Lamp P, de la Casa-Lillo MA. J Phys Chem B 1998;102:10894–8.
[102] Feynman RP, Hibbs A. Quantum mechanics and path integrals. New York: McGraw-Hill; 1965.
[103] Docherty H, Galindo A, Vega C, Sanz E. J Chem Phys 2006;125(7):074510.
[104] Guan P, Mckenzie DR, Pailthorpe BA. J Phys: Condens Matter 1996;8:8753–62.
[105] Filippova VP, Kunavin SA, Pugachev MS. Inorg Mater Appl Res 2015;6:1–4.
[106] Rappé AK, Casewit CJ, Colwell KS, Goddard III WA, Skiff WM. J Am Chem Soc 1992;114:10024–35.
[107] Arkundato A, Su'ud Z, Sudarko, Hasan M, Celino M. J Phys: Conf Ser 2015;622:012009.
[108] Singer K, Taylor A, Singer JVL. Mol Phys 1977;33:1757–95.
[109] Sebesta F, Sláma V, Melcr J, Futera Z, Burda JV. J Chem Theory Comput 2016;12:3681–8.
[110] Reif MM, Hünenberger PH. J Chem Phys 2011;134:144104.
[111] Mayo SL, Olafson BD, Goddard III WA. J Phys C: Solid State Phys 1990;94:8897–909.
[112] Tribe L, Manning M, Morgan JA, Stephens MD, Ronk WR, Treptow E, et al. J Phys Chem B 1998;102:206–11.
[113] Ponce V, Galvez-Aranda DE, Seminario JM. J Phys Chem C 2017;121:12959–71.
[114] Mardiyah RU, Arkundato A, Misto, Purwandari E. J Phys: Conf Ser 2020;1491:012020.
[115] Cheung PSY, Powles JG. Mol Phys 1975;30:921–49.
[116] Jorgensen WL, Madura JD, Swenson CJ. J Am Chem Soc 1984;106:6638–46.
[117] Soper A. Pramana J Phys 2004;63:41–50.
[118] Beyer O, Hoheisel C. Z. Nat.forsch. A 1983;38:859–65.
[119] Cambridge Crystallographic Database Centre. 2023, www.ccdc.cam.ac.uk. [Accessed 2 January 2024].
[120] Li A, Bueno R, Wiggin S, Ward SC, Wood PA, Fairen-Jimenez D. Matter 2021;4:1090–106.
[121] Kokalj A. Comput Mater Sci 2003;28:155–68.
[122] Zhou W, Wu H, Hartman MR, Yildirim T. J Phys Chem C 2007;111(44):16131–7.

[123] Collins DJ, Zhou H-C. J Mater Chem 2007;17:3154–60.
[124] Yang SJ, Kim T, Im JH, Kim YS, Lee K, Jung H, et al. Chem Mater 2012;24(3):464–70.
[125] Langmi HW, Ren J, North B, Mathe M, Bessarabov D. Electrochim Acta 2014;128:368–92.
[126] Saha D, Bao Z, Jia F, Deng S. Environ Sci Technol 2010;44(5):1820–6.
[127] Ursueguía D, Díaz E, nez SO. Sci Total Environ 2021;790:148211.
[128] Spanopoulos I, Tsangarakis C, Klontzas E, Tylianakis E, Froudakis G, Adil K, et al. J Am Chem Soc 2016;138(5):1568–74.
[129] Wu H, Zhou W, Yildirim T. J Am Chem Soc 2009;131(13):4995–5000.
[130] Senkovska I, Kaskel S. Microporous Mesoporous Mater 2008;112(1):108–15.
[131] Alezi D, Jia J, Bhatt PM, Shkurenko A, Solovyeva V, Chen Z, et al. Inorg Chem 2022;61(28):10661–6.
[132] Pei X, Bürgi H-B, Kapustin EA, Liu Y, Yaghi OM. J Am Chem Soc 2019;141(47):18862–9.
[133] Feyand M, Mugnaioli E, Vermoortele F, Bueken B, Dieterich JM, Reimer T, et al. Angew Chem Int Edn 2012;51(41):10373–6.
[134] Ovsyannikov AS, Noamane MH, Abidi R, Ferlay S, Solovieva SE, Antipin IS, et al. CrystEngComm 2016;18:691–703.
[135] Du Y, Zhong L, Hu Y, Li Q, Qian J. CrystEngComm 2019;21:5045–9.
[136] Karsch M, Lund H, Schulz A, Villinger A, Voss K. Eur J Inorg Chem 2012;2012(33):5542–53.
[137] Luo X, Kan L, Li X, Sun L, Li G, Zhao J, et al. Cryst Growth Des 2016;16(12):7301–7.
[138] Yao S, Xu T, Zhao N, Zhang L, Huo Q, Liu Y. Dalton Trans 2017;46:3332–7.